LETTER

Quantum back-action-evading measurement of motion in a negative mass reference frame

Christoffer B. Møller[1]*, Rodrigo A. Thomas[1]*, Georgios Vasilakis[1,2], Emil Zeuthen[1,3], Yeghishe Tsaturyan[1], Mikhail Balabas[1,4], Kasper Jensen[1], Albert Schliesser[1], Klemens Hammerer[3] & Eugene S. Polzik[1]

Quantum mechanics dictates that a continuous measurement of the position of an object imposes a random quantum back-action (QBA) perturbation on its momentum. This randomness translates with time into position uncertainty, thus leading to the well known uncertainty on the measurement of motion[1,2]. As a consequence of this randomness, and in accordance with the Heisenberg uncertainty principle, the QBA[3,4] puts a limitation—the so-called standard quantum limit—on the precision of sensing of position, velocity and acceleration. Here we show that QBA[5] on a macroscopic mechanical oscillator can be evaded if the measurement of motion is conducted in the reference frame of an atomic spin oscillator[6,7]. The collective quantum measurement on this hybrid system of two distant and disparate oscillators is performed with light. The mechanical oscillator is a vibrational 'drum' mode of a millimetre-sized dielectric membrane[8], and the spin oscillator is an atomic ensemble in a magnetic field[9,10]. The spin oriented along the field corresponds to an energetically inverted spin population and realizes a negative-effective-mass oscillator, while the opposite orientation corresponds to an oscillator with positive effective mass. The QBA is suppressed by −1.8 decibels in the negative-mass setting and enhanced by 2.4 decibels in the positive-mass case. This hybrid quantum system paves the way to entanglement generation and distant quantum communication between mechanical and spin systems and to sensing of force, motion and gravity beyond the standard quantum limit.

Continuous measurement of an oscillator position, $\hat{x}(t) = \hat{x}(0)\cos(\Omega t) + \hat{p}(0)\sin(\Omega t)/(m\Omega)$, where Ω is the frequency and m is the mass, leads to accumulation of the QBA of the measurement in both position and momentum, $\hat{p}$, which are non-commuting variables $[\hat{x}, \hat{p}] = i\hbar$ (refs 1, 2). Measurement QBA was recently observed for a mechanical oscillator[3] and for atomic motion[4]. Suppose, however, that the position is measured relative to an oscillator with a mass $m_0 = -m$ for which $\dot{\hat{x}}_0 = -\hat{p}_0/m$. The result of a measurement of $\hat{x}(t) - \hat{x}_0(t) = (\hat{x}(0) - \hat{x}_0(0))\cos(\Omega t) + (\hat{p}(0) + \hat{p}_0(0))\sin(\Omega t)/(m\Omega)$ depends only on commuting variables, $[\hat{x} - \hat{x}_0, \hat{p} + \hat{p}_0] = 0$. Hence it can be QBA-free[6,7], and the uncertainty in the measurement of the relative position $\langle(\hat{x} - \hat{x}_0)^2\rangle$ can be smaller than the uncertainty $\langle\hat{x}^2\rangle$. The first proposal for such a measurement based on atomic spins[7] was followed by a number of proposals for QBA-free measurements[11–15]. In ref. 16, the negative mass approach referred to as "quantum-mechanics-free subsystems" was shown to unite a quantum non-demolition measurement, back-action evasion and coherent noise cancellation. Earlier work on atomic spin ensembles used the negative mass property for demonstration of entanglement of macroscopic spins[17] and for entanglement-assisted magnetometry[18]. The back-action-evading measurement on two mechanical oscillators at room temperature was demonstrated in ref. 19 in the classical regime using light, and recently in the quantum regime in the millikelvin temperature range using microwaves[20]. Ways

to overcome QBA limitations for a free mass oscillator with squeezed light have been proposed[21–23].

Here we demonstrate QBA evasion in a novel hybrid quantum system[24,25] composed of a macroscopic mechanical oscillator and a spin oscillator. The former is a high-Q dielectric membrane[5,8] (Fig. 1a and Methods) placed in a high-finesse optical cavity, and the latter is an ensemble of near room temperature caesium atoms in a magnetic field contained in a spin-protecting environment[9,10,26] (see Fig. 1b and Methods). The mechanical oscillator Hamiltonian is $\hat{H}_M = (m\Omega_M^2/2)\hat{x}^2 + \hat{p}^2/2m = (\hbar\Omega_M/2)(\hat{X}_M^2 + \hat{P}_M^2)$, where we henceforth employ dimensionless variables $\hat{X}_M = \hat{x}/x_{zpf}$ and $\hat{P}_M = \hat{p}x_{zpf}/\hbar$, where $x_{zpf} = \sqrt{\hbar/m\Omega_M}$ is the oscillator's zero point position fluctuation, Ω_M its frequency, and $[\hat{X}_M, \hat{P}_M] = i$. Compared to a mechanical oscillator, a spin oscillator has some unique properties. Consider a collective atomic spin $\hat{J}_\alpha = \sum_{i=1}^{N_S} \hat{F}_\alpha^i$ with components $\alpha = x, y, z$, composed of a large number N_S of ground state spins $\hat{F}^i$ (with $F^i = 4$ in the present case). Atoms are optically pumped to generate an energetically inverted spin population in an external magnetic field B (Fig. 1c), which we take to point in the positive x-direction. The collective spin thus exhibits a large average projection $J_x = |\langle \hat{J}_x \rangle|/\hbar \gg 1$. Its normalized y, z quantum components form canonical oscillator variables $[\hat{X}_S, \hat{P}_S] = [\hat{J}_z/\sqrt{\hbar J_x}, -\hat{J}_y/\sqrt{\hbar J_x}] = i$ (ref. 9) in terms of which the spin Hamiltonian becomes $\hat{H}_S = \hbar\Omega_S\hat{J}_x = \hbar\Omega_S J_x - (\hbar\Omega_S/2)(\hat{X}_S^2 + \hat{P}_S^2)$ where Ω_S is the Larmor frequency. The first term is an irrelevant constant energy offset due to the mean spin polarization. The second term is equivalent to the Hamiltonian of a mechanical oscillator $\hat{H}_M$ with a negative mass. Each quantum of excitation in the negative mass spin oscillator physically corresponds to a de-excitation of the inverted spin population by $\hbar\Omega_S$ (Fig. 1c). Preparation of the collective spin in the energetically lowest Zeeman state realizes instead a positive mass spin oscillator with $\hat{H}_S = -\hbar\Omega_S J_x + (\hbar\Omega_S/2)(\hat{X}_S^2 + \hat{P}_S^2)$ (Fig. 1d).

The experiment implementing a quantum measurement on the hybrid system is sketched in Fig. 2a, which depicts the cascaded interaction between a travelling light field and the two oscillators (see Methods for details). A coherent optical field with a strong, classical, linearly polarized component LO$_1$ (photon flux Φ_1) and vacuum quantum fluctuations in the polarization orthogonal to it, described by quadrature phase operators $\hat{X}_{L,in}$ and $\hat{P}_{L,in}$, first interacts with the spin oscillator. The interaction for far-off-resonant light is of the quantum non-demolition type $\hat{H}_{int,S} \propto \hat{X}_S\hat{X}_{L,in}$, where $\hat{X}_S \propto \hat{J}_z$ is the projection of the collective spin on the direction of light propagation[9]. The light output quadrature, $\hat{P}_{L,out}^S(\Omega) = \hat{P}_{L,in}(\Omega) + \sqrt{\Gamma_S}\hat{X}_S(\Omega)$, reads out the atomic spin projection $\hat{X}_S$ at the rate $\Gamma_S \propto \Phi_1$. At the same time $\hat{H}_{int,S}$ implies that measurement QBA due to $\hat{X}_{L,in}$ is imprinted on the atomic $\hat{P}_S$ quadrature. The atomic spin projection is driven in addition by intrinsic spin noise $\hat{F}_S$ so that
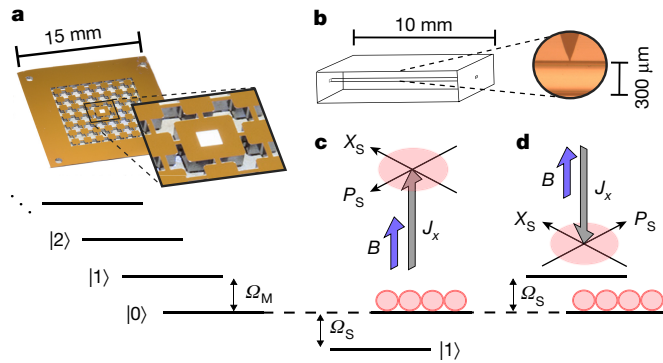
Figure 1 | Mechanical and spin oscillators. a, Top, the mechanical oscillator is the (1,2) drum mode, with frequency $\Omega_M = 2\pi \times 1.28\,MHz$, of a $0.5\,mm \times 0.5\,mm \times 60\,nm$ silicon nitride membrane, shown as the light square in the centre of the inset. It is supported by a silicon phononic crystal structure. Bottom, phononic energy level structure, with the ground state aligned (dashed line) with the energy levels into which the atomic spin oscillator is initiated. **b**, The spin oscillator is an optically pumped gas of caesium atoms contained in a square-cross-section channel inside a glass cell. The channel walls are coated with a spin-protecting coating. Inset, detail of the channel, including the funnel connecting it to the reservoir containing caesium vapour. The cell is placed in a static magnetic field, giving rise to an energy splitting with Larmor frequency Ω_S, tunable around Ω_M. Depending on the direction of the magnetic field B with respect to the direction of the atomic spin J_x, the oscillator can have a lower (higher) excited-state energy, corresponding to a negative (positive) effective mass, as shown in **c** (**d**). X_S and P_S are the canonical position and momentum spin variables, respectively, defining the phase space of the spin oscillator (black coordinate systems), in which free evolution corresponds to rotation around the magnetic field vector **B** according to the right-hand rule. Areas in pink represent the ground state noise of the atomic spin ensemble.

$\hat{X}_S = \chi_S(\Omega)[\sqrt{\gamma_S}\hat{F}_S + \sqrt{\Gamma_S}\hat{X}_{L,in}]$. Here and henceforth we consider all quantities in the Fourier (frequency) domain, which is most appropriate for a continuous-time measurement. The atomic oscillator's susceptibility $\chi_S(\Omega) = \pm 2\Omega_S/(\Omega_S^2 - \Omega^2 - 2i\Omega\gamma_S)$ is determined by the sign of its effective mass ($\pm$), resonance frequency Ω_S and relaxation rate γ_S (the half-width at half-maximum convention is used throughout this Letter). The physics of the QBA in the spin system can be understood as fluctuations of the Stark shift of the atomic energy levels due to quantum fluctuations of the angular momentum of light[9].

The classical drive LO$_1$ is filtered out after light passes through the atoms (Fig. 2a), whereas the relevant fluctuations in the orthogonal polarization, $\hat{P}_{L,out}^S$ and $\hat{X}_{L,out}^S = \hat{X}_{L,in}$, are mixed with a classical drive field LO$_2$ (with photon flux Φ_2) in the same polarization and sent onto the mechanical oscillator. The phase of LO$_2$ is adjusted so that $\hat{X}_{L,in}^M = \hat{X}_{L,out}^S$ and $\hat{P}_{L,in}^M = \hat{P}_{L,out}^S$. The linearized optomechanical Hamiltonian is $\hat{H}_{int,M} \propto \hat{X}_M \hat{X}_{L,in}^M$ (ref. 27). By analogy with the spin, the output phase quadrature of light, $\hat{P}_{L,out} = \hat{P}_{L,in}^M + \sqrt{\Gamma_M}\hat{X}_M$, reads out the membrane position $\hat{X}_M$ at the rate $\Gamma_M \propto \Phi_2$. The membrane position is driven by thermal state noise $\hat{F}_M$ and the QBA of light, that is, $\hat{X}_M = \chi_M(\Omega)[\sqrt{\gamma_{M0}}\hat{F}_M + \sqrt{\Gamma_M}\hat{X}_{L,in}^M]$, where the mechanical susceptibility is given by $\chi_M(\Omega) = 2\Omega_M/(\Omega_M^2 - \Omega^2 - 2i\Omega\gamma_{M0})$ and determined by the mechanical resonance frequency Ω_M and damping rate γ_{M0}. Hence $\hat{X}_{L,in}$ is the source of measurement QBA for both the membrane and the spin oscillator.

Overall, the homodyne readout of the joint system with the local oscillator LO$_3$ (Fig. 2a) can be cast as $\hat{P}_{L,out} = \hat{P}_{L,in} + \sqrt{\Gamma_M}\hat{X}_M + \sqrt{\Gamma_S}\hat{X}_S$. The back-action-evading character of this measurement comes out most clearly when the measured light quadrature for the joint system is expressed as $\hat{P}_{L,out} = \hat{P}_{L,in} + \sqrt{\Gamma_M\gamma_{M0}}\chi_M(\Omega)\hat{F}_M + \sqrt{\Gamma_S\gamma_S}\chi_S(\Omega)\hat{F}_S + [\Gamma_M\chi_M(\Omega) + \Gamma_S\chi_S(\Omega)]\hat{X}_{L,in}$, with the terms on the right hand side

corresponding to shot noise of light, membrane thermal noise, spin noise, and measurement QBA noise, respectively. Notably, the QBA term shows the interfering responses of the membrane and the spin oscillator. Ideal broadband QBA evasion is achieved for equal readout rates, $\Gamma_S = \Gamma_M$, and $\chi_M(\Omega) = -\chi_S(\Omega)$, which requires $\Omega_M = \Omega_S$, $\gamma_{M0} = \gamma_S$ and a negative mass spin oscillator (Methods and ref. 12).

We exploit the high level of flexibility in our modular hybrid set-up to fulfil these requirements. It is straightforward to match the readout rates $\Gamma_M \approx \Gamma_S$ by a proper choice of power levels $\Phi_{1,2}$, and to tune the atomic Larmor frequency Ω_S to the mechanical resonance frequency Ω_M of the mechanical drum mode. In order to observe appreciable QBA at the membrane's thermal environment of 7 K, we use a phononic-bandgap shielded membrane with high mechanical quality factor Q corresponding to an intrinsic damping rate of $\gamma_{M0} = 2\pi \times 50\,mHz$. On the other hand, the intrinsic spin damping rate $\gamma_{S0} \approx 2\pi \times 500\,Hz$ is due to power broadening by optical pumping and atomic collisions. In addition, efficient spin readout requires substantial power broadening by the probe light, $\gamma_S \gg \gamma_{S0}$ (Methods), impeding an adjustment of the spin to the mechanical linewidth. Instead we optically broaden the mechanical linewidth by introducing a detuning $\Delta < 0$ of LO$_2$ from the cavity resonance. This is a well established technique in optomechanical sideband cooling experiments which exploits the dynamical back-action of light on the mechanical oscillator, changing the mechanical susceptibility by causing a considerably enhanced effective damping rate $\gamma_M \gg \gamma_{M0}$ (ref. 27), while modifying the resonance frequency by $<1\%$ ($\Omega_M \rightarrow 2\pi \times 1.27\,MHz$). In this way matched linewidths $\gamma_M \approx \gamma_S$ can be achieved by a proper choice of Φ_2 and Δ (compare Fig. 2c, d). The experimental parameters are listed in Extended Data Table 1. Introducing a non-zero detuning also modifies the optomechanical input–output relations and the QBA interference, as detailed further below and in the Methods.

The ratio of QBA from vacuum noise of light $\hat{X}_{L,in}$ to thermal noise due to $\hat{F}_{M(S)}$ is proportional to the quantum cooperativity parameters $C_q^{M(S)}$, respectively, which we separately calibrate for each system (Methods). We achieve an optomechanical cooperativity of $C_q^M = 2.6 \pm 0.3$ and for the atomic spin system $C_q^S = 1.10 \pm 0.15$, which signifies that QBA and thermal noise contribute on the same level in both systems (Fig. 2c, d).

With similar susceptibilities, readout rates and QBA contributions of the two systems, we perform a back-action-limited readout of the hybrid system with the spin system contribution reduced by propagation losses, see Fig. 3. As a reference, we show in Fig. 3a the spectra of the two individual systems taken separately (blue, the mechanics; orange, the spin), both measured with the LO$_3$ detector. Figure 3b presents the hybrid noise for the negative (red) and positive (green) effective spin masses, corresponding to two opposite orientations of the DC magnetic field relative to the spin polarization. The hybrid spectra differ substantially from each other, with the area of the spectrum for the negative (positive) spin mass being significantly smaller (larger) than that for uncorrelated systems—a clear demonstration of the destructive (constructive) interference of the QBA contributions for the two systems. We emphasize that these data signify a QBA cancellation irrespective of theoretical modelling. For comparison, Fig. 3a also shows the curve (dashed) obtained by adding the two noise spectra recorded in separate measurements on atoms and the mechanical oscillator.

An intriguing feature of the hybrid noise spectra is the apparent absence of interference and noise cancellation exactly at the Fourier frequency $\Omega = \Omega_S = \Omega_M$, where the joint negative, joint positive and the mechanics spectra overlap (Fig. 3b). This is due to the strong optical broadening of the mechanical oscillator, which leads to suppression of the spin phase noise contribution to light on the exact joint resonance. The effect is well understood from the full quantum model (Methods) and is analogous to optomechanically induced transparency[28]. In Fig. 3 the solid red, green and blue curves for the negative joint, positive joint and mechanics, respectively, are generated from this model and are in excellent agreement with the data. Figure 3c presents the
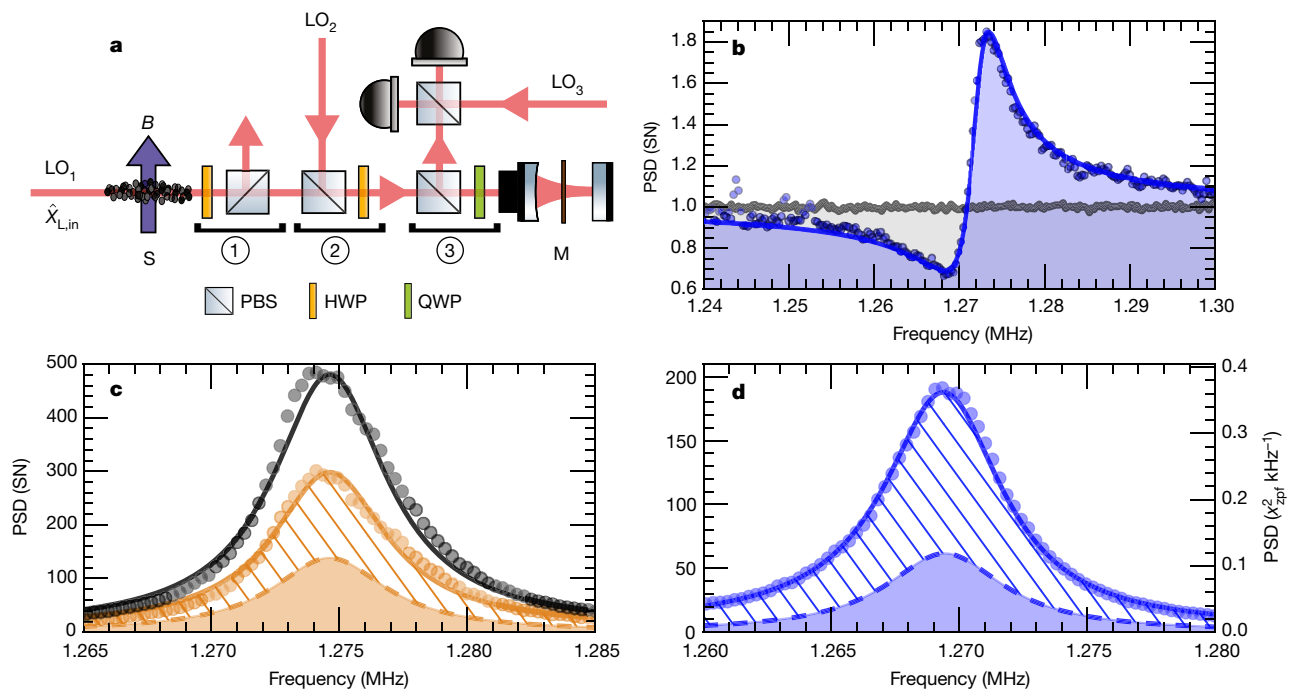
Figure 2 | Experimental set-up and observation of QBA for the spin and mechanical oscillators. a, Simplified experimental set-up. Atomic spin ensemble S in magnetic field B is probed by the field LO_1. The mechanical oscillator M is probed by LO_2. For both systems, the quadrature $\hat{X}_{L,in}$ is the QBA force. PBS, polarizing beam splitter; HWP, half-wave plate; QWP, quarter-wave plate. Circled numerals show sections with the following functions: (1) removes LO_1; (2) introduces LO_2 with an appropriate phase and polarization; (3) collects the output of optomechanical cavity for homodyning with LO_3. See text for details. **b**, Light amplitude quadrature power spectral density (PSD) of the optomechanical system (blue dots) and light shot noise (grey). Solid blue line, model fit. Regions are shaded for illustrative purposes. **c**, Light phase quadrature PSD of the spin system. Grey dots, spin driven with white light noise and thermal force; orange dots, spin driven by light vacuum noise (shot noise) and thermal force;

orange dashed curve and shaded area, thermal noise of the spin; striped area, QBA determined from the data, solid lines, full model. **d**, Light phase quadrature PSD of optomechanical system (blue dots) driven by vacuum light noise (shot noise) and thermal force. Blue dashed curve and shaded area, membrane thermal noise; striped area, QBA determined from squeezing data shown in **b**. In **c** and **d**, as in Fig. 3, left-hand y axis is PSD in units of shot noise (SN), right-hand y axis is PSD in units of x_{zpf}^2 (zero point fluctuations). The variance of the shot noise is white, and constitutes the noise floor whose mean value is used as a unit on the left-hand axis. Similarly, the variance of the zero point fluctuations of the mechanical oscillator produces a metric by which to measure the mechanical motional variance imprinted on the output light variance. All displayed noise spectra derive from >1,000 time traces (Fourier transformed and then averaged).

spectrum for the hybrid system with the negative mass and the model fit (blue curve) to the spectrum of the mechanics (data in Fig. 3a). The noise reduction of the hybrid spectrum (red dots) compared to the mechanics only (blue curve) in the wings of the spectrum is observable, although its effect is diminished by the added spin thermal noise which is present in the red data, but does not contribute to the blue curve. The observed variance (spectral area) for the joint negative system is $2.9 \times x_{zpf}^2$, which is 95% $\pm$ 2% of the observed variance for the mechanical oscillator, where the error is derived from the fits. For the positive spin mass, the constructive interference of the QBA for the two systems is evident from comparing the green data points to the blue curve for the membrane only (Fig. 3d).

To find the reduction/enhancement of the QBA for the hybrid system, we use the calibration of the thermal noise described in the Methods and presented in Fig. 2c, d. The mechanical thermal noise found in Fig. 2d is shown as the blue shaded area in Fig. 3c, d. The spin thermal noise found in Fig. 2c is used as an input to the detailed model to find its contribution to the observed hybrid spectra (orange shaded area in Fig. 3c, d). Note that this noise is suppressed by the optomechanical response around $\Omega_M = \Omega_S$ by the same mechanism as the QBA contribution of the spin is reduced to zero at this point. Subtracting the thermal noise area from the total area, we find the QBA variance contribution for the hybrid negative system to be $1.5 \times x_{zpf}^2$ (striped area in Fig. 3c) and for the hybrid positive system, $3.1 \times x_{zpf}^2$ (striped area in Fig. 3d). Comparing these values with the QBA of $2.0 \times x_{zpf}^2$ for the mechanical oscillator, we conclude that the variance of the QBA for

the joint negative mass system is $-1.2\,dB$ (24% $\pm$ 5%) below the variance for the mechanics alone, whereas for the joint positive mass system it is $1.9\,dB$ (53% $\pm$ 8%) higher. The main contributions to the uncertainties lie in the calibration of quantum cooperativities.

Further studies reveal that a more efficient QBA evasion can be achieved when the two oscillator frequencies are not exactly equal, $\Omega_M \neq \Omega_S$. Taking advantage of the straightforward tunability of Ω_S with magnetic field, we ran the QBA evasion experiment with the spin oscillator slightly detuned from the mechanical oscillator. In this case, the best QBA evasion is obtained if the quadratures of light between the atomic and the optomechanical systems are rotated with respect to the phase of LO_2. Figure 4a shows the data for the hybrid system with the negative spin mass (red dots) with $\Omega_S - \Omega_M = 2\pi \times 4.2\,kHz$ and a phase rotation of 6°, along with the noise of the mechanical oscillator (blue dots). For this experiment we find $C_q^M = 2.2$. We observe the broadband QBA evasion which, additionally, is most pronounced at $\Omega = \Omega_M$ where the mechanical response is maximal. The observed total variance for the hybrid system with the negative spin mass, $2.6 \times x_{zpf}^2$, is 94% $\pm$ 2% of the variance for membrane only, $2.8 \times x_{zpf}^2$. Note that interference in the hybrid system leads to suppression of the spin noise (solid orange curve) at Ω_S, which is instead transformed into efficient QBA evasion around Ω_M for the negative mass hybrid system. Figure 4b shows the improvement in the membrane displacement sensitivity obtained by the QBA evasion calculated as the ratio of the blue and red curves from Fig. 4a. These data signify broadband QBA evasion in a model independent way.
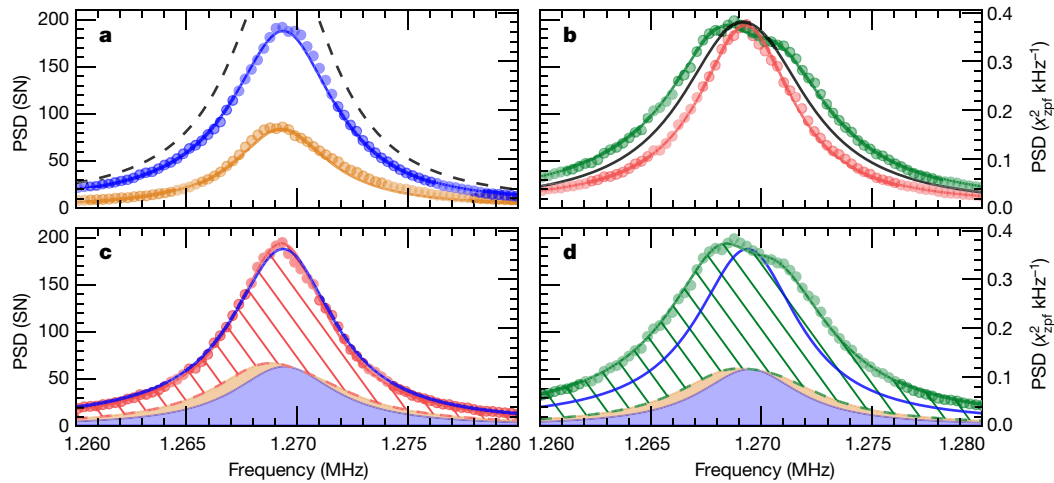
Figure 3 | QBA interference for the mechanical and spin oscillators with equal central frequencies. a, Light phase quadrature PSD of mechanical oscillator, blue dots; spin oscillator, orange dots; the sum of the two spectra, black dashed line. **b**, Hybrid spectrum for the system with the negative (red dots) and positive (green dots) effective mass spin oscillator. Black curve, the model for the joint noise spectrum of the hybrid system with QBA interference put to zero. **c, d**, Hybrid spectrum noise for the negative (**c**, red dots) and positive (**d**, green dots) effective mass spin oscillator. Shown also are the thermal noise of the membrane (blue shaded area), the thermal noise of the spin (orange shaded area) and the joint thermal noise (**c**, red dashed curve; **d**, green dashed curve). Striped area shows QBA of the hybrid system; blue curve, model fitted to the membrane noise data (same as in **a**). All solid curves show the results of the full model (Methods). All displayed noise spectra derive from >1,000 time traces (Fourier transformed and then averaged).

Subtracting thermal noise contributions, we find the hybrid QBA (red shaded area in Fig. 4a) of $1.1 \times x_{zpf}^2$, that is, $-1.8\,\text{dB}$ ($34\% \pm 5\%$) suppression compared to the mechanical QBA of $1.7 \times x_{zpf}^2$ (striped area). For the hybrid system with the positive spin mass (green dots), the QBA is $3.0 \times x_{zpf}^2$, which is $2.4\,\text{dB}$ ($73\% \pm 10\%$) above the QBA for the mechanics alone. In this detuned case, the QBA reduction obtained in the case of negligible thermal noise can, in principle, overcome the limit of 1/2 that is valid for the case of $\Omega_M = \Omega_S$ (see Methods), as indicated by the 60% reduction of the classical back-action that we have observed in an independent experiment (not shown) with the system driven by classical white noise. The physics of the broadband QBA interference is due to the combination of the frequency dependent

amplitude squeezing of the light generated by the spin and the interference of the QBA of the two systems. An example of the amplitude squeezed output from the spin is shown in Fig. 4c.

We have presented a novel hybrid quantum system consisting of spatially separated mechanical and spin oscillators linked by propagating photons. Constructive or destructive interference of the QBA for the two oscillators (depending on the sign of the effective mass of the spin oscillator) is demonstrated. A detailed model describes the results with high accuracy. We have shown that the back-action-evading measurement in the hybrid system leads to an enhancement of displacement sensitivity. Further improvements are realistic prospects, such as reduced propagation losses, even higher-Q mechanical
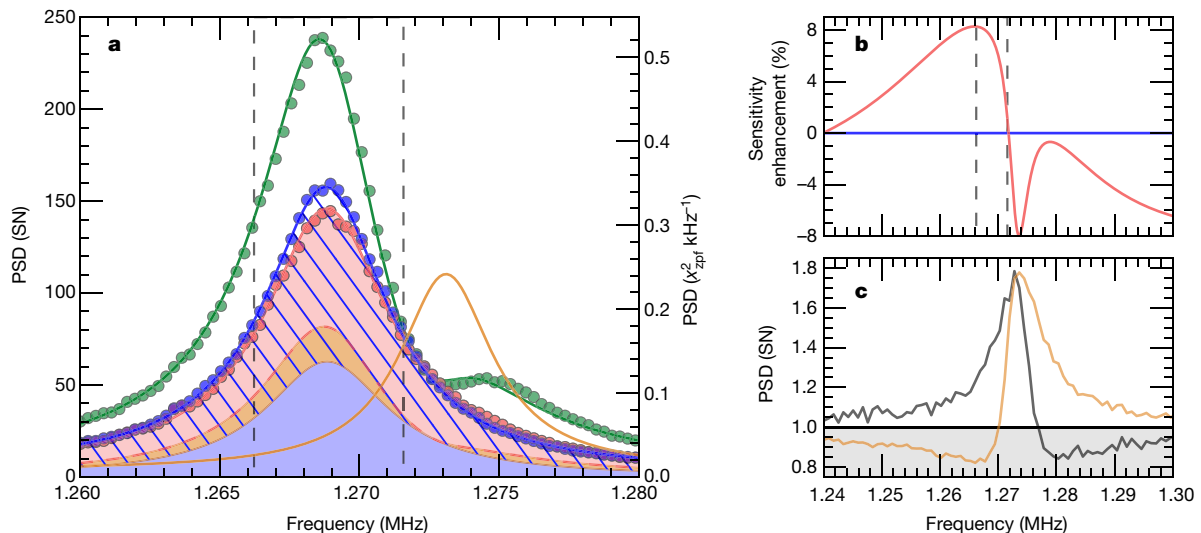

Figure 4 | QBA evasion for the optimally detuned mechanical and spin oscillators. a, Light phase quadrature PSD of membrane noise (blue dots); hybrid system with the negative/positive effective mass spin oscillator (red/green dots); blue area, membrane thermal noise; orange area, spin thermal noise; solid orange line, a fit to the experimental spin spectrum taken without mechanical response; red area, QBA for the hybrid system; striped area, QBA for the membrane. Dashed vertical black lines (also displayed in **b**) indicate the full-width at half-maximum ($2\gamma_M$) frequency range of the mechanical response. **b**, Displacement sensitivity for the hybrid system with the negative effective mass spin oscillator (red) normalized to the sensitivity for the mechanical oscillator. **c**, An example of the squeezed amplitude output of the spin system for the positive (black) and negative (orange) effective mass spin oscillator. All displayed noise spectra derive from >1,000 time traces (Fourier transformed and then averaged).

oscillators (ref. 29) and cavity-enhanced spin systems. Our results pave the way to entanglement generation and quantum communication between mechanical and spin systems, and to QBA-free measurements of acceleration, gravity and force.

1. Caves, C. M., Thorne, K. S., Drever, R. W. P., Sandberg, V. D. & Zimmermann, M. On the measurement of a weak classical force coupled to a quantum-mechanical oscillator. I. Issues of principle. *Rev. Mod. Phys.* **52,** 341–392 (1980).
2. Braginsky, V. B., Vorontsov, Y. I. & Thorne, K. S. Quantum nondemolition measurements. *Science* **209,** 547–557 (1980).
3. Purdy, T. P., Peterson, R. W. & Regal, C. A. Observation of radiation pressure shot noise on a macroscopic object. *Science* **339,** 801–804 (2013).
4. Spethmann, N., Kohler, J., Schreppler, S., Buchmann, L. & Stamper-Kurn, D. M. Cavity-mediated coupling of mechanical oscillators limited by quantum back-action. *Nat. Phys.* **12,** 27–31 (2016).
5. Nielsen, W. H. P., Tsaturyan, Y., Møller, C. B., Polzik, E. S. & Schliesser, A. Multimode optomechanical system in the quantum regime. *Proc. Natl Acad. Sci. USA* **114,** 62–66 (2017).
6. Polzik, E. S. & Hammerer, K. Trajectories without quantum uncertainties. *Ann. Phys.* **527,** A15–A20 (2015).
7. Hammerer, K., Aspelmeyer, M., Polzik, E. S. & Zoller, P. Establishing Einstein-Podolsky-Rosen channels between nanomechanics and atomic ensembles. *Phys. Rev. Lett.* **102,** 020501 (2009).
8. Tsaturyan, Y. *et al.* Demonstration of suppressed phonon tunneling losses in phononic bandgap shielded membrane resonators for high-Q optomechanics. *Opt. Express* **22,** 6810–6821 (2014).
9. Hammerer, K., Sørensen, A. S. & Polzik, E. S. Quantum interface between light and atomic ensembles. *Rev. Mod. Phys.* **82,** 1041–1093 (2010).
10. Vasilakis, G. *et al.* Generation of a squeezed state of an oscillator by stroboscopic back-action-evading measurement. *Nat. Phys.* **11,** 389–392 (2015).
11. Tsang, M. & Caves, C. M. Coherent quantum-noise cancellation for optomechanical sensors. *Phys. Rev. Lett.* **105,** 123601 (2010).
12. Bariani, F., Seok, H., Singh, S., Vengalattore, M. & Meystre, P. Atom-based coherent quantum-noise cancellation in optomechanics. *Phys. Rev. A* **92,** 043817 (2015).
13. Zhang, K., Meystre, P. & Zhang, W. Back-action-free quantum optomechanics with negative-mass Bose-Einstein condensates. *Phys. Rev. A* **88,** 043632 (2013).
14. Woolley, M. J. & Clerk, A. A. Two-mode back-action-evading measurements in cavity optomechanics. *Phys. Rev. A* **87,** 063846 (2013).
15. Motazedifard, A., Bemani, F., Naderi, M. H., Roknizadeh, R. & Vitali, D. Force sensing based on coherent quantum noise cancellation in a hybrid optomechanical cavity with squeezed-vacuum injection. *New J. Phys.* **18,** 073040 (2016).
16. Tsang, M. & Caves, C. M. Evading quantum mechanics: engineering a classical subsystem within a quantum environment. *Phys. Rev. X* **2,** 031016 (2012).
17. Julsgaard, B., Kozhekin, A. & Polzik, E. S. Experimental long-lived entanglement of two macroscopic objects. *Nature* **413,** 400–403 (2001).
18. Wasilewski, W. *et al.* Quantum noise limited and entanglement-assisted magnetometry. *Phys. Rev. Lett.* **104,** 133601 (2010).
19. Caniard, T., Verlot, P., Briant, T., Cohadon, P.-F. & Heidmann, A. Observation of back-action noise cancellation in interferometric and weak force measurements. *Phys. Rev. Lett.* **99,** 110801 (2007).
20. Ockeloen-Korppi, C. F. *et al.* Quantum backaction evading measurement of collective mechanical modes. *Phys. Rev. Lett.* **117,** 140401 (2016).
21. Unruh, W. G. *Quantum Noise in the Interferometer Detector* 647–660 (Springer US, 1983).
22. Kimble, H. J., Levin, Y., Matsko, A. B., Thorne, K. S. & Vyatchanin, S. P. Conversion of conventional gravitational-wave interferometers into quantum nondemolition interferometers by modifying their input and/or output optics. *Phys. Rev. D* **65,** 022002 (2001).
23. Danilishin, S. L. & Khalili, F. Y. Quantum measurement theory in gravitational-wave detectors. *Living Rev. Relativ.* **15,** 5 (2012).
24. Kurizki, G. *et al.* Quantum technologies with hybrid systems. *Proc. Natl Acad. Sci. USA* **112,** 3866–3873 (2015).
25. Jöckel, A. *et al.* Sympathetic cooling of a membrane oscillator in a hybrid mechanical-atomic system. *Nat. Nanotechnol.* **10,** 55–59 (2015).
26. Seltzer, S. J. & Romalis, M. V. High-temperature alkali vapor cells with antirelaxation surface coatings. *J. Appl. Phys.* **106,** 114905 (2009).
27. Aspelmeyer, M., Kippenberg, T. J. & Marquardt, F. Cavity optomechanics. *Rev. Mod. Phys.* **86,** 1391–1452 (2014).
28. Weis, S. *et al.* Optomechanically induced transparency. *Science* **330,** 1520–1523 (2010).
29. Tsaturyan, Y., Barg, A., Polzik, E. S. & Schliesser, A. Ultra-coherent nanomechanical resonators via soft clamping and dissipation dilution. *Nat. Nanotechnol.* http://dx.doi.org/10.1038/nnano.2017.101 (2017).

METHODS

Experimental set-up. *Atomic spin oscillator.* The spin ensemble consists of $N_S \approx 10^9$ caesium atoms contained in an anti-relaxation-coated Pyrex vapour cell (microcell)[30] heated to a temperature of 65 °C. These atoms are confined in a channel of $300\,\mu m \times 300\,\mu m \times 10\,mm$ connected to an external caesium reservoir via a $\sim 10\,\mu m$ radius laser drilled hole, as shown in Fig. 1b. They are addressed by light of waist (radius) size $55\,\mu m$ focused through the channel. The microcell is enclosed in a four layer magnetic shielding, protecting the spins from ambient magnetic fields and external RF sources. An inner system of coils produces a homogeneous bias field, B, which leads to a Larmor frequency Ω_S. The wall-to-wall transient time of caesium atoms in the channel is on average about $1.5\,\mu s$. Within the characteristic evolution time of the quantum state, the moving atoms have to cross the light beam many times, experiencing a motionally averaged interaction[9,31]; atoms that do not satisfy this condition contribute to an uncorrelated broadband feature added to the spins' phase response. In the experiments described in this Letter, this contribution is an additional approximately 2.5 shot noise units. The spin-protecting coating of the cell walls grants an intrinsic decoherence rate of about $300\,\mu s$. This rate is limited by spin destruction collisions of atoms with the cell walls, magnetic field inhomogeneities and spin-exchange collisions.

A circularly polarized diode laser tuned to the $F = 3 \rightarrow F' = 4$ transition of the D2 line is used to spin-polarize atoms into the $F = 4$ ground state. The probing of the atomic ensemble is done with linearly polarized light at 852.3490 nm (LO$_1$), blue detuned by $\Delta_S \approx 2\pi \times 3\,GHz$ from the $F = 4 \rightarrow F' = 5$ transition of the D2 line. Absorption effects can be neglected as $\Delta_S \gg \Delta\omega_{Doppler}^{HWHM} \approx 2\pi \times 200\,MHz$, effectively eliminating the effect of spin motion. The polarization of the probe set by the half-wave plate (HWP$_0$ in Extended Data Fig. 1) allows for adjustment of the polarization axis of the linearly polarized probing light (LO$_1$). In the experiment this axis is chosen to minimize the added broadening of the spin oscillator, resulting in an angle $\theta_S \approx 55°$ with respect to the direction of the atomic polarization. We emphasize that the dominant part of the light–atoms interaction is of the quantum non-demolition type (see equation (18)) and does not depend on the angle θ_S; the optical rotation that the light experiences is to a very good approximation independent of the polarization orientation. The atoms experience a very inhomogeneous intensity distribution of light (due to the Gaussian profile of the beam) and may experience an effective inhomogeneous oscillator frequency as they move across the cell due to the light-shift. This light-shift is proportional to the photon flux and the tensor polarizability and scales with the orientation of the light polarization axis as $(1 + 3\cos 2\theta_S)$. The vacuum sidebands that affect the spin oscillator are in an orthogonal polarization mode and $\pi/2$ out of phase with respect to the local oscillator LO$_1$.

The optical readout rate, $\Gamma_S \propto \Delta_S^{-2} \Phi_1 |J_x|$, is a function of the number of atoms $J_x = FN_S$, the local oscillator photon flux Φ_1 and the detuning Δ_S. Its origin lies in the re-parameterization of the Faraday rotation experienced by light due to interaction with far-detuned atoms[10,32]. In the established language of the light–atoms interface[9], the readout rate is related to the interaction strength $\kappa_{atoms}^2 = \Gamma_S T$, with T being the temporal length of the probing light mode. The atomic spins' linewidth, γ_S, is dominated by the optical broadening and is proportional to Φ_1 in the regime of interest. Typical values for optical powers and γ_S are presented in Extended Data Table 1.

The caesium spin ensemble fully polarized to $F = 4$, $m_F = \pm 4$ has projection noise variance $\mathrm{var}(\hat{J}_{y,z})_{PN} = |J_x|\hbar/2 = FN_S\hbar/2 = 2N_S\hbar$ in its ground state, whereas a completely unpolarized ensemble has $\mathrm{var}(\hat{J}_{y,z})_{Th} = F(F+1)N_S\hbar/3 = 10/3 \times \mathrm{var}(\hat{J}_{y,z})_{PN}$ (ref. 9). In the experiment $\mathrm{var}(\hat{J}_{y,z}) \approx 2.8 \times \mathrm{var}(\hat{J}_{y,z})_{PN}$ with the degree of spin polarization of 60%, equivalent to having 1.8 units of extra ground state noise. The negative (positive) mass configuration is achieved by optical pumping of the atoms to the $F = 4$, $m_F = +4$ ($F = 4$, $m_F = -4$) state, that is, parallel (antiparallel) to the magnetic field, which we take to define the positive x-direction. Within the Holstein-Primakoff approximation[33] this is formally equivalent to having a harmonic oscillator with $\Omega_S < 0$ ($\Omega_S > 0$) as depicted in Fig. 1c (Fig. 1d) in the main text. Note that throughout the Methods, we include the sign of the effective spin mass in Ω_S (whereas this sign is stated as an explicit prefactor in the main text). For the negative (positive) mass oscillator, the first excited state of the spin oscillator is the one with a single atom in the $F = 4$, $m_F = 3$ ($F = 4$, $m_F = -3$) state. Experimentally, we change the magnetic field direction to choose the sign of the oscillator's mass.

As presented in Fig. 2c, the quantum cooperativity for the spin oscillator, C_q^S, is characterized via broadband white noise modulation of the optical driving force. This technique requires an electro-optical modulator to drive LO$_1$'s polarization quadrature $\hat{X}_{L,in}$ and a RF source outputting white voltage noise, producing a frequency independent (and proportional to the driving voltage). optical power with excess n_{WN} photon flux in the frequency band of interest. In Fig. 2c, the black

dots represent the spin oscillator driven with $n_{WN} = 1.22$. Comparing this curve to the shot-noise limited ($n_{WN} = 0$) probing, in orange dots, we extract the effect of quantum noise of light on the spin oscillator and the ratio of back-action to thermal noise, the quantum cooperativity. For a thorough discussion on this we refer to Methods section 'Calibration of QBA for the spin system'.

Optomechanical system. The optomechanical system is based on a near-monolithic cryogenic membrane-in-the-middle system[5]. The mechanical oscillator is a highly stressed, 60 nm thick stoichiometric silicon nitride (SiN) membrane supported by a silicon periodic structure forming a phononic bandgap. The bandgap protects the oscillator from phonon tunnelling from the clamping of the structure and provides a region clear of undesired phononic modes[8]. The high stress boosts the quality factor through dissipation dilution[29]. The membrane thickness, t_M, is chosen to maximize the optomechanical single photon coupling rate, g_0. The trade-off is between the zero point fluctuations $x_{zpf} = \sqrt{\hbar/(m_{eff}\Omega_M)} \propto t_M^{-1/2}$ and the amplitude reflection coefficient of SiN, which is periodic with t_M. The coupling g_0 depends linearly on both of these quantities.

The (1,2) drum mode of the membrane with an intrinsic frequency $\Omega_{M0} = 2\pi \times 1.28\,MHz$ is used because it is the lowest frequency mode to lie within the bandgap and has a high quality factor of $Q = 13 \times 10^6$ as measured by ring-downs ($\gamma_{M0} = 2\pi \times 50\,mHz$). The approximately 8% side length difference of the membrane breaks the degeneracy of the (1,2) and (2,1) modes, with the (1,2) mode being about 60 kHz lower in frequency than its sibling. This membrane is placed in a cavity and aligned such that the cavity TEM$_{00}$ mode has a good overlap with the (1,2) mode and a poor overlap with the (2,1) mode. This further separates the systems as the optical spring effect (dynamical back-action) pushes the (1,2) mode another $\sim 10\,kHz$ away, while having only a marginal impact on the (2,1) mode.

The 1.3 mm long plano-concave Fabry-Pérot optical cavity with finesse $F = 4,500$ (half bandwidth of $\kappa = 2\pi \times 13\,MHz$) is mounted in a continuous flow cryostat with large windows for good optical access and a base temperature of 4.4 K. The power transmissions of the mirrors are 20 p.p.m. and 1,400 p.p.m., thus producing a largely one-sided cavity. Placing the aforementioned dielectric membrane $500\,\mu m$ from the 20 p.p.m. mirror forms two sub-cavities, whose dynamics can be mapped onto the canonical optomechanical formulation used in the theory section via the transfer matrix model approach described in ref. 34. In effect, the cavity half-bandwidth κ and coupling rate g_0 are modulated depending on the position of the membrane with respect to the standing wave in the cavity[35]. This is due to a differential intracavity power in each sub-cavity. Having more intracavity power in the sub-cavity bounded on one side by the low transmission (20 p.p.m.) mirror produces an overall decreased cavity loss rate. In the canonical formulation, this is equivalent to the decay rates κ_1 and κ_2 of the cavity ports 1 and 2 being altered asymmetrically, see Extended Data Fig. 2. The membrane itself adds negligible additional intracavity loss.

The membrane is positioned in the cavity such that the coupling rate is large and the overall cavity bandwidth reduced from $\kappa = 2\pi \times 13\,MHz$ (bare cavity) to $\kappa = 2\pi \times 7.7\,MHz$ (finesse enhanced to 7,500). This comes at the expense of having a less one-sided cavity. The ratio of the cavity ports decay rates goes from $\kappa_1/\kappa_2 = 70$ (bare cavity) to $\kappa_1/\kappa_2 = 25$. The reduced cavity bandwidth is advantageous, as a certain degree of sideband resolution is required to optically broaden the mechanical oscillator sufficiently without requiring a too large readout rate (necessary to match the spin system).

The high transmission incoupling mirror is mounted on a piezoelectric transducer, which is used to tune the cavity resonance frequency close to that dictated by the atomic probe LO$_1$. It is tuned such that LO$_2$ probes the cavity red detuned by $\Delta = -2\pi \times 4.7\,MHz$. This is ensured using a separate beam originating from the same laser. This beam is blue shifted (by $-\Delta$) from LO$_2$ described above by an acousto-optic modulator. It is then phase modulated at 12 MHz and probes the cavity from the undercoupled port 2, see Extended Data Fig. 1. An error signal is derived using the Pound-Drever-Hall technique and is used to feedback on the aforementioned piezoelectric transducer which stabilizes the cavity such that this beam is locked on resonance. This locking beam is in the orthogonal polarization to LO$_2$ and contributes to <1% of the intracavity power. The locking beam thus has a negligible impact on the intracavity dynamics and the final detection.

The mechanical oscillator is initially only coupled to a thermal bath of temperature T_{bath} with mean occupation $\bar{n}_{bath}$. Adding the probe LO$_2$ alters the dynamics of the system, as the oscillator is coupled to the intracavity field with a rate $g = g_0\sqrt{N}$, where N is the mean intracavity photon number. Dynamical back-action optically broadens the mechanical linewidth by $\gamma_{M,opt}$ (such that $\gamma_M = \gamma_{M0} + \gamma_{M,opt}$) and the mean thermal occupation is reduced to $\bar{n}_M^{th} = (\gamma_{M0}/\gamma_M)\bar{n}_{bath}$. This (so-called) sideband cooling is due to an asymmetry in the Stokes and anti-Stokes processes caused by the detuning from cavity resonance. The Stokes sideband (causing heating) is never completely suppressed, which sets a minimum achievable mean occupation $\bar{n}_M^{min}$ (ref. 36). The effective mean occupation of the mechanical

oscillator is now $\bar{n}_M = (\gamma_{M0}/\gamma_M)\bar{n}_{bath} + (\gamma_{M,opt}/\gamma_M)\bar{n}_M^{min}$, where the contribution $\bar{n}_M^{min}$ is correlated with the QBA.

The total variance of motion will thus have contributions from both the QBA and the thermal bath; the ratio of these is

$$\frac{\gamma_{M,opt}(\bar{n}_M^{min} + 1/2)}{\gamma_{M0}(\bar{n}_{bath} + 1/2)} \approx \frac{C_q^M}{2}\left(\frac{\kappa^2}{\kappa^2 + (\Delta - \Omega_M)^2} + \frac{\kappa^2}{\kappa^2 + (\Delta + \Omega_M)^2}\right) \quad (1)$$

where we have introduced the quantum cooperativity $C_q^M = g_0^2 N/(2\kappa\gamma_{M0}\bar{n}_{bath})$ and approximated $\bar{n}_{bath} + 1/2 \approx \bar{n}_{bath}$ (in the present scenario $\bar{n}_{bath} \approx 10^5$). The observed ratio of QBA to thermal noise contributions also depends on the detected quadrature being observed, with equation (1) being a very good approximation for the phase quadrature data presented in Figs 2–4.

The total variance of the motion can be directly inferred from the area of the measured output spectrum by $\langle \hat{X}_M^2 \rangle = \int (\Gamma_M^{-1}\langle \hat{P}_{L,out}^2 \rangle - 1)d\Omega \approx \Gamma_M^{-1} \int \langle \hat{P}_{L,out}^2 \rangle d\Omega$. The approximation is good as the spectra used are dominated by QBA and thermal noise contributions, with a negligible SN contribution, in the frequency range shown in all figures. By the same token, equation (1) gives operational meaning to the quantum cooperativity C_q^M as the ratio of QBA and thermal contributions to the observed variance (except for the Lorentzian factor of order unity, $\lesssim 1$, seen on the right-hand side).

The optomechanical system is probed in reflection. The combination of a quarter-wave plate at 45° and a polarizing beam splitter effectively acts as an isolator transmitting the input light (in the hybrid configuration coming from the spin system) and reflecting the light emerging from the cavity. With well characterized optical losses and system parameters, the bath temperature and C_q^M can be inferred from the observed degree of ponderomotive squeezing. A spectrum (amplitude quadrature) showing squeezing of -1.7 dB (-2.6 dB corrected for detection efficiency of 72%) is shown in Fig. 2b. The SN level is verified by balanced detection and by comparison to a white light source to within <5% accuracy. Using the detailed model (outlined in the theory section) with the bath temperature of the membrane, T_{bath}, as the only adjustable parameter, we obtain the fit shown in Fig. 2b with $T_{bath} = (7 \pm 0.5)$ K. From T_{bath} we thus obtain the value of $C_q^M = 2.6 \pm 0.3$ for the data presented in Fig. 2d. The thermal noise contribution is shown as the blue area and can easily be found using equation (1).

For the two phase quadrature data sets shown the mechanical oscillator was optically broadened to $\gamma_M \approx 2\pi \times 2.7$ kHz. This required the input LO$_2$ power to be adjusted as the cavity half-bandwidth and single photon coupling rate varied slightly between runs. This was due to a varying membrane position with respect to the intra-cavity field on different days caused by overnight temperature cycles. The experimentally realized parameters for these are displayed in Extended Data Table 1.

Mirror substrate noise (as can be seen as spikes in the low frequency wing of Fig. 2b) is not modelled as its contribution is negligible compared to SN in the relevant frequency range. The closest mirror substrate modes are about $5\gamma_M$ away, thus rendering their impact minor. Their added decoherence would decrease the fraction of the QBA contribution to the total mechanical variance, thus increasing the QBA reduction claimed in the main text.

Hybrid system. A detailed schematic of the experimental set-up is shown in Extended Data Fig. 1: a travelling light field interacts with the atomic spin and the mechanical oscillator in a cascaded way. The driving beams for the system, LO$_1$ and LO$_2$, as well as the local oscillator LO$_3$ for the homodyne measurement, are generated by a Ti-sapphire laser. The light is SN limited for the relevant powers and Fourier frequencies of interest in the quadratures that matter for both systems.

The spin-mechanics interface requires filtering of the spins' output field. The atomic spins respond to modulation out of phase and in the orthogonal polarization to its local oscillator (denoted by the quantum field operator $\hat{X}_{L,in}$ in the main text). The mechanical oscillator responds to modulation in phase and in the same polarization mode as its own driving local oscillator (represented by the field operator $\hat{X}_{L,in}^M$). Therefore, LO$_2$ should be in an orthogonal polarization mode and $\pi/2$ phase shifted with respect to LO$_1$. Two filtering stages are required, one for polarization and one for phase, both of them being depicted in Extended Data Fig. 1 and described in the following. The polarization filtering is done using HWP$_1$ and PBS$_1$ right after the microcell, decoupling LO$_1$ from the quantum fluctuations of interest in the orthogonal polarization quadrature; the phase filtering is realized using a Mach–Zehnder interferometer with output at PBS$_2$, setting a variable phase for the spin sideband fields $\{\hat{X}_{L,out}^S, \hat{P}_{L,out}^S\}$ with respect to LO$_2$. The driving local oscillator and the sidebands are then projected in the same polarization mode with HWP$_3$ and PBS$_3$ and coupled to the optomechanical cavity. To detect the optical quadrature of interest, balanced polarimetry with the local oscillator LO$_3$ (with the aid of another Mach–Zehnder interferometer) is performed when the phase

quadrature is of interest; to measure the amplitude quadrature, the local oscillator is removed and all light is directed to a single photodiode. In the experiment, PBS$_1$ extinguishes LO$_1$ better than 1:10^3 from the optical path with little loss of the modulation sidebands or those carrying information about the spin oscillator.

An electro-optic modulator (EOM) in LO$_1$ is used for locking the phase filtering interferometer. The phase and axis of the EOM are adjusted in such a way that a voltage modulation (small with respect to the π voltage) results in a small modulation predominantly in the degree of circular polarization of light (quantified by the $\hat{S}_z$ Stokes component). The ratio of circular polarization modulation to linear polarization modulation introduced by the EOM is typically about 10^5 in power. Sinusoidal modulation sidebands at 10 MHz, far from both oscillators' responses, provide the phase reference. These sidebands are combined with LO$_2$ in the output of the interferometer, PBS$_2$. A half-wave plate allows for an adjustable fraction of the sideband power to be used for locking (typically about 5%). The demodulated result of the balanced polarimetry measurement of the locking signal in D$_1$ is proportional to $\cos\delta\phi_{LO_{1,2}}$, where $\delta\phi_{LO_{1,2}}$ is the phase difference between LO$_1$ and LO$_2$. Feedback on a piezoelectric transducer proportional to this signal allows us to lock the new local oscillator in phase with the sideband quadrature that drove the spin oscillator.

The half-wave plate HWP$_2$ and PBS$_2$ project a small portion of LO$_2$ (approximately 3%) and most of the sideband signal (about 97%) into the same polarization mode. Suitable optics direct the beam onto the optomechanical cavity with a total optical power transmission for the spin system response sidebands in the 60%–65% range. These sidebands are in the same spatial mode as LO$_1$, which is mode-matched to the cavity with an efficiency of $\eta_{mm} \approx 90\%$ The mode-matching is defined as the fraction of incident LO$_1$ power going into the TEM$_{00}$ mode compared to all TEM modes.

When the characterization of the atomic spin oscillator is performed, a function generator provides a white noise (WN) modulation over the frequency range of interest, from 1 MHz to 2 MHz; typical values for the added modulated WN photons (in units of SN) range from 0.5 to 100.

The spectra of $\hat{P}_{L,out}$ are measured by balanced homodyning of the field reflected off the optomechanical cavity with LO$_3$, with power of the order of 1.5 mW, which is locked to the DC zero of the interference fringe with LO$_2$, thus ensuring that the phase quadrature is being measured.

The model fits and knowledge of all relevant system parameters provide a reliable reference point from which we calibrate the spectra in units of the mechanical zero point fluctuations. For example, the right vertical axis in Fig. 2d shows the spectral density of motion in units of x_{zpf}^2 kHz^{-1}, calibrated to the thermal noise variance contribution in the presence of optical cooling. Integrating the power spectral density data, we find the observed mechanical variance of $3.0 \times x_{zpf}^2$. Subtracting the thermal noise variance of $1.0 \times x_{zpf}^2$, we obtain the QBA variance $2.0 \times x_{zpf}^2$.

Losses in the system are due to the finite transmission coefficient between the spin and the optomechanical systems of $\eta_1 = 61\%$ and the finite optomechanical cavity mode-matching efficiency $\eta_{mm} = 89\%$. Detection losses are given by the transmission coefficient between the optomechanical system and the detection of $\eta_2 \approx 64\%$ which includes the quantum efficiency of the photodetector and the mode-matching to the homodyning LO$_3$. These values vary within a few percentage points from experiment to experiment.

Theoretical model. *Optomechanical system.* The optomechanical system is described by the standard linearized Hamiltonian

$$\hat{H} = \frac{\Omega_M}{2}(\hat{X}_M^2 + \hat{P}_M^2) - \Delta\hat{a}^\dagger\hat{a} - g(\hat{a}e^{-i\phi} + \hat{a}^\dagger e^{i\phi})\hat{X}_M$$

where $[\hat{X}_M, \hat{P}_M] = i$ are the dimensionless canonical operators for the mechanical system with frequency Ω_M, and $[\hat{a}, \hat{a}^\dagger] = 1$ are annihilation/creation operators for cavity photons. $\Delta = \omega_L - \omega_c$ is the detuning of the driving laser from the cavity resonance ω_c. The linearized optomechanical coupling rate $g = g_0|\alpha|$ depends on the single photon coupling rate g_0 of the optomechanical system and the intracavity amplitude α. It is linked to the optomechanical readout rate Γ_M introduced in the main text by

$$\Gamma_M = \frac{2g^2}{\kappa} \quad (2)$$

where κ is the cavity half linewidth. The phase $\phi = \arctan(\Delta/\kappa)$ denotes the phase of the intracavity field amplitude α relative to driving field, as is discussed further below in connection with equation (32). Here we take the incoming field as the phase reference instead of the intracavity field (as is usually done in cavity optomechanics) since we are eventually interested in the transfer matrix for the incoming/outgoing amplitudes resulting from this Hamiltonian. Including decay

and Langevin noise forces, the equations of motion corresponding to the Hamiltonian are

$$\dot{\hat{a}}(t) + (\kappa - i\Delta)\hat{a}(t) - ige^{i\phi}\hat{X}_M(t) = \sqrt{2\kappa_1}\,\hat{a}_{in}(t) + \sqrt{2\kappa_2}\,\hat{v}_{in}(t)$$

$$\ddot{\hat{X}}_M(t) + \Omega_M^2\hat{X}_M(t) + 2\gamma_{M0}\dot{\hat{X}}_M(t) - \Omega_M g(\hat{a}(t)e^{-i\phi} + \hat{a}^\dagger(t)e^{i\phi}) = \sqrt{4\gamma_{M0}}\,\Omega_M\hat{f}(t)$$

where $\hat{a}_{in}(t)$ and $\hat{v}_{in}(t)$ are incoming quantum fields driving the cavity through port 1 and 2, respectively, compare Extended Data Fig. 2; their commutation relations are $[\hat{a}_{in}(t),\hat{a}_{in}^\dagger(t')] = \delta(t - t') = [\hat{v}_{in}(t),\hat{v}_{in}^\dagger(t')]$. The partial decay rates $\kappa_{1(2)}$ fulfil $\kappa = \kappa_1 + \kappa_2$. The linewidth of the mechanical resonance (excluding optical broadening) is γ_{M0}, and the thermal Langevin force is $\hat{f}(t)$. In the high temperature limit we can take $\langle\hat{f}(t)\hat{f}(t')\rangle = \delta(t - t')(\bar{n}_{bath} + 1/2)$ where $\bar{n}_{bath} \approx k_B T_{bath}/(\hbar\Omega_M)$.

In the frequency domain, the equations of motion read

$$(\kappa - i(\Delta + \Omega))\hat{a}(\Omega) - ige^{i\phi}\hat{X}_M(\Omega) = \sqrt{2\kappa_1}\,\hat{a}_{in}(\Omega) + \sqrt{2\kappa_2}\,\hat{v}_{in}(\Omega)$$

$$D_{M0}(\Omega)\hat{X}_M(\Omega) - g\Omega_M(\hat{a}(\Omega)e^{-i\phi} + \hat{a}^\dagger(-\Omega)e^{i\phi}) = \sqrt{4\gamma_{M0}}\,\Omega_m\hat{f}(\Omega)$$

where

$$D_{M0}(\Omega) = \Omega_M^2 - \Omega^2 - 2i\Omega\gamma_{M0} \tag{3}$$

We define field quadratures as

$$\hat{X}_L(\Omega) = \frac{1}{2}(\hat{a}(\Omega) + \hat{a}^\dagger(-\Omega)), \quad \hat{P}_L(\Omega) = \frac{1}{2i}(\hat{a}(\Omega) - \hat{a}^\dagger(-\Omega)) \tag{4}$$

and similar definitions are used for quadratures of incoming/outgoing fields. In terms of these the equations of motion in frequency domain are

$$\begin{pmatrix} \kappa - i\Omega & \Delta & g\sin\phi \\ -\Delta & \kappa - i\Omega & -g\cos\phi \\ -2g\Omega_M\cos\phi & -2g\Omega_M\sin\phi & D_{M0}(\Omega) \end{pmatrix}\begin{pmatrix} \hat{X}_L(\Omega) \\ \hat{P}_L(\Omega) \\ \hat{X}_M(\Omega) \end{pmatrix}$$

$$= \begin{pmatrix} \sqrt{2\kappa_1}\,\hat{X}_{L,in}^M(\Omega) + \sqrt{2\kappa_2}\,\hat{V}_{x,in}(\Omega) \\ \sqrt{2\kappa_1}\,\hat{P}_{L,in}^M(\Omega) + \sqrt{2\kappa_2}\,\hat{V}_{p,in}(\Omega) \\ \sqrt{4\gamma_{M0}}\,\Omega_M\hat{f}(\Omega) \end{pmatrix}$$

which can be conveniently written in terms of block matrices

$$\begin{pmatrix} O_\phi & 0 \\ 0 & 1 \end{pmatrix}\begin{pmatrix} A & B \\ C & D_{M0}(\Omega) \end{pmatrix}\begin{pmatrix} O_\phi^T & 0 \\ 0 & 1 \end{pmatrix}\begin{pmatrix} \hat{X}_L(\Omega) \\ \hat{X}_M(\Omega) \end{pmatrix} = \begin{pmatrix} \sqrt{2\kappa_1}\,\hat{X}_{L,in}^M(\Omega) + \sqrt{2\kappa_2}\,\hat{V}_{in}(\Omega) \\ \sqrt{4\gamma_{M0}}\,\Omega_M\hat{f}(\Omega) \end{pmatrix}$$

where

$$O_\phi = \begin{pmatrix} \cos(\phi) & -\sin(\phi) \\ \sin(\phi) & \cos(\phi) \end{pmatrix}, \quad A = \begin{pmatrix} \kappa - i\Omega & \Delta \\ -\Delta & \kappa - i\Omega \end{pmatrix},$$

$$B = \begin{pmatrix} 0 \\ -g \end{pmatrix}, \quad C = (-2g\Omega_M \quad 0), \quad \hat{X}_L(\Omega) = \begin{pmatrix} \hat{X}_L(\Omega) \\ \hat{P}_L(\Omega) \end{pmatrix}, \quad \text{etc.}$$

The equations of motion are solved by

$$\begin{pmatrix} \hat{X}_L(\Omega) \\ \hat{X}_M(\Omega) \end{pmatrix} = \begin{pmatrix} O_\phi & 0 \\ 0 & 1 \end{pmatrix}\begin{pmatrix} A & B \\ C & D_{M0}(\Omega) \end{pmatrix}^{-1}\begin{pmatrix} O_\phi^T & 0 \\ 0 & 1 \end{pmatrix}\begin{pmatrix} \sqrt{2\kappa_1}\,\hat{X}_{L,in}^M(\Omega) + \sqrt{2\kappa_2}\,\hat{V}_{in}(\Omega) \\ \sqrt{4\gamma_{M0}}\,\Omega_M\hat{f}(\Omega) \end{pmatrix}$$

where the inverse block matrix can be expressed in two equivalent forms

$$\begin{pmatrix} A & B \\ C & D_{M0}(\Omega) \end{pmatrix}^{-1} = \begin{pmatrix} A^{-1} + A^{-1}BS^{-1}CA^{-1} & -A^{-1}BS^{-1} \\ -S^{-1}CA^{-1} & S^{-1} \end{pmatrix} \tag{5}$$

$$= \begin{pmatrix} T^{-1} & -T^{-1}BD_{M0}^{-1} \\ -D_{M0}^{-1}CT^{-1} & D_{M0}^{-1} + D_{M0}^{-1}CT^{-1}BD^{-1} \end{pmatrix} \tag{6}$$

by means of the Schur complements:

$$S = D_{M0}(\Omega) - CA^{-1}B = D_{M0}(\Omega) + \frac{\Gamma_M\kappa\Omega_M\Delta}{(\kappa - i\Omega)^2 + \Delta^2} =: D_M(\Omega) \tag{7}$$

$$T = A - BD_{M0}^{-1}(\Omega)C = \begin{pmatrix} \kappa - i\Omega & \Delta \\ -\Delta - \frac{\Gamma_M\kappa\Omega_M}{D_{M0}(\Omega)} & \kappa - i\Omega \end{pmatrix} \tag{8}$$

The effective mechanical susceptibility including optically induced shift and broadening is:

$$\chi_M(\Omega) = 2\Omega_M D_M^{-1}(\Omega) \tag{9}$$

The intracavity quadratures following from equations (5) and (6) are

$$\hat{X}_L(\Omega) = O_\phi T^{-1}O_\phi^T\left(\sqrt{2\kappa_1}\,\hat{X}_{L,in}^M(\Omega) + \sqrt{2\kappa_2}\,\hat{V}_{in}(\Omega)\right)$$

$$+ \frac{\sqrt{2\gamma_{M0}\kappa\Gamma_M}\,\Omega_m}{D_M(\Omega)}O_\phi A^{-1}\hat{F}(\Omega)$$

in which

$$\hat{F}(\Omega) := \begin{pmatrix} 0 \\ \hat{f}(\Omega) \end{pmatrix}$$

and the field reflected off the cavity in port 1 is:

$$\hat{X}_{L,out}^M(\Omega) = -\hat{X}_{L,in}^M(\Omega) + \sqrt{2\kappa_1}\,\hat{X}_L(\Omega)$$

$$= O_\phi(2\kappa_1 T^{-1} - 1)O_\phi^T\hat{X}_{L,in}^M(\Omega) + \sqrt{4\kappa_1\kappa_2}\,O_\phi T^{-1}O_\phi^T\hat{V}_{in}(\Omega)$$

$$+ \frac{2\sqrt{\Gamma_M\kappa\kappa_1\gamma_{M0}}\,\Omega_m}{D_M(\Omega)}O_\phi A^{-1}\hat{F}(\Omega) \tag{10}$$

$$=: \mathbb{M}(\Omega)\hat{X}_{L,in}^M(\Omega) + \mathbb{V}(\Omega)\hat{V}_{in}(\Omega) + \mathbb{F}(\Omega)\hat{F}(\Omega)$$

The optomechanical transfer matrix $\mathbb{M}(\Omega)$ is explicitly given by

$$\mathbb{M}(\Omega) = \frac{2\kappa_1}{(\kappa - i\Omega)^2 + \Delta\left(\Delta + \frac{\Gamma_M\kappa\Omega_M}{D_{M0}(\Omega)}\right)}O_\phi\begin{pmatrix} \kappa - i\Omega & -\Delta \\ \Delta + \frac{\Gamma_M\kappa\Omega_M}{D_{M0}(\Omega)} & \kappa - i\Omega \end{pmatrix}O_\phi^T - 1$$

$$= \frac{1}{D_c(\Omega)}\frac{2\kappa_1 D_{M0}(\Omega)}{D_M(\Omega)}O_\phi\begin{pmatrix} \kappa - i\Omega & -\Delta \\ \Delta + \frac{\Gamma_M\kappa\Omega_M}{D_{M0}(\Omega)} & \kappa - i\Omega \end{pmatrix}O_\phi^T - 1 \tag{11}$$

where $D_c(\Omega) = (\kappa - i\Omega)^2 + \Delta^2$. In the form given in the second line, the dependence on the effective mechanical susceptibility becomes evident.

We note that for a broadband cavity ($\kappa \gg \Delta, \Omega_M, \Omega$) and neglecting losses ($\kappa_2 = 0$) one recovers from equation (10) the simple optomechanical input–output relation stated in the main text:

$$\begin{pmatrix} \hat{X}_{L,out}^M(\Omega) \\ \hat{P}_{L,out}^M(\Omega) \end{pmatrix} = \begin{pmatrix} 1 & 0 \\ \Gamma_M\chi_M(\Omega) & 1 \end{pmatrix}\begin{pmatrix} \hat{X}_{L,in}^M(\Omega) \\ \hat{P}_{L,in}^M(\Omega) \end{pmatrix} + \sqrt{\Gamma_M\gamma_{M0}}\,\chi_M(\Omega)\begin{pmatrix} 0 \\ \hat{f}(\Omega) \end{pmatrix} \tag{12}$$

In the limit considered here, the susceptibility corresponds to that of the bare mechanical system (without shift and broadening).

For non-zero detuning and taking into account effects of a finite cavity linewidth, the more involved input–output relations described by equations (10) have to be considered in general. However, in the unresolved-sideband regime ($\kappa \gg \Omega_M, \Omega$) we may obtain a simplified expression for the optomechanical transfer matrix, equation (11). To this end, we note that the cavity response to the individual sideband components at $\pm\Omega$ of the light quadratures, equation (4), is governed by the complex Lorentzian

$$L(\Omega) = \frac{\kappa}{\kappa - i(\Delta + \Omega)} =: |L(\Omega)|e^{i\theta(\Omega)},$$

$$|L(\Omega)| = \frac{\kappa}{\sqrt{\kappa^2 + (\Delta + \Omega)^2}}, \quad \theta(\Omega) = \arctan\left(\frac{\Delta + \Omega}{\kappa}\right) \tag{13}$$

where we have introduced its polar decomposition. In terms of this, equation (11) can be reexpressed as (again neglecting cavity losses for simplicity, $\kappa_2 = 0$)

$$\mathbb{M}(\Omega) = e^{i[\theta(\Omega) - \theta(-\Omega)]} O_{\phi + [\theta(\Omega) + \theta(-\Omega)]/2}$$
$$\left[\left[1 + i\frac{\Gamma_{\mathrm{M}}\chi_{\mathrm{M}}(\Omega)}{4}(|L(\Omega)|^2 - |L(-\Omega)|^2)\right]\mathbb{1}\right.$$
$$\left.+ \frac{\Gamma_{\mathrm{M}}\chi_{\mathrm{M}}(\Omega)}{4}\begin{pmatrix} 0 & (|L(\Omega)| + |L(-\Omega)|)^2 \\ \Gamma_{\mathrm{M}}\chi_{\mathrm{M}}(\Omega) & 1 \end{pmatrix}\right] \quad (14)$$
$$O^{\mathrm{T}}_{\phi - [\theta(\Omega) + \theta(-\Omega)]/2}$$

where $\phi = \theta(0)$ (see discussion of equation (32) below) and $\chi_{\mathrm{M}}(\Omega)$ is the effective mechanical susceptibility, equation (9). To obtain a simpler expression for equation (14) in the regime $\kappa \gg \Omega_{\mathrm{M}}, \Omega$, we expand $|L(\Omega)|$ and $\theta(\Omega)$ to linear order around the carrier frequency ($\Omega = 0$ in the rotating frame)

$$|L(\Omega)| \approx L_0 + \delta L(\Omega), L_0 := |L(0)| = \frac{\kappa}{\sqrt{\kappa^2 + \Delta^2}},$$
$$\delta L(\Omega) := -\frac{\Omega\Delta\kappa}{(\kappa^2 + \Delta^2)^{3/2}} \quad (15)$$

$$\theta(\Omega) \approx \phi + \delta\theta(\Omega), \quad \delta\theta(\Omega) := \frac{\Omega\kappa}{\kappa^2 + \Delta^2} \quad (16)$$

resulting in the optomechanical scattering matrix

$$\mathbb{M}(\Omega) \approx e^{2i\delta\theta(\Omega)} O_{2\phi}\left(\left[1 + i\Gamma_{\mathrm{M}}\chi_{\mathrm{M}}(\Omega)L_0\delta L(\Omega)\right]\mathbb{1} + \Gamma_{\mathrm{M}}\chi_{\mathrm{M}}(\Omega)L_0^2\begin{pmatrix} 0 & 0 \\ 1 & 0 \end{pmatrix}\right) \quad (17)$$

to leading order in $\delta\theta$, δL (the phase prefactor does not affect the resulting spectra and will be suppressed for brevity henceforth). The transfer matrix in equation (17) interpolates between the simple result in equation (12), which is valid in the limit $\kappa \to \infty$, and the general result in equation (11).

When considering the field reflected off the cavity in port 1 in equation (10), the finite mode-matching η_{mm} of the input quadratures $\hat{\boldsymbol{X}}_{\mathrm{L,in}}(\Omega)$ to the cavity quadratures $\hat{\boldsymbol{X}}_{\mathrm{L}}(\Omega)$ is treated as equivalent to the input port having higher loss, that is, $\kappa_1 \to \eta_{\mathrm{mm}}\kappa_1$. The total cavity loss remains fixed $\kappa = \kappa_1 + \kappa_2$ and we simply treat $\kappa_2 \to \kappa_2 + (1 - \eta_{\mathrm{mm}})\kappa_1$ as the input for the additional vacuum noise.

Atomic spin system. As discussed in refs 9, 10, in the limit of low saturation and large detuning from the atomic resonance, the Hamiltonian affecting the atomic spin and light polarization observables can be written in the form:

$$\hat{H}_{\mathrm{int}} = \alpha\hat{S}_z\hat{J}_z \quad (18)$$

where $\hat{J}_z$ is the dimensionless ($\hbar = 1$) collective spin component along the direction of light propagation (taken here to coincide with the z axis in the laboratory frame) and $\hat{S}_z$ is the Stokes component of light that measures the degree of circular polarization. The parameter α depends on the detuning from the resonance Δ_{S}, on the area A of interaction and on physical constants:

$$\alpha = \frac{\Gamma_{\mathrm{sp}}}{8A\Delta_{\mathrm{S}}}\frac{\lambda^2}{2\pi}\alpha_1(\Delta_{\mathrm{S}}) \quad (19)$$

where Γ_{sp} is the spontaneous emission rate associated with the optical transition, λ is the wavelength of light and $\alpha_1(\Delta_{\mathrm{S}})$ is a numerical factor that depends on the specific atomic structure and for detunings much larger than the excited state hyperfine structure can be approximated to be unity.

For an ensemble of a large number of atoms, highly polarized along the direction of a static magnetic field (x direction), the Holstein-Primakoff transformation can be performed and maps the collective spin operators to position and momentum operators of an effective (spin) oscillator:

$$\hat{X}_{\mathrm{S}} = \frac{\hat{J}_z}{\sqrt{|J_x|}}; \quad \hat{P}_{\mathrm{S}} = -\mathrm{sgn}(J_x)\frac{\hat{J}_y}{\sqrt{|J_x|}} \quad (20)$$

Here we represent the macroscopic mean polarization by its x-projection $J_x = \langle\hat{J}_x\rangle$ (including its sign) rather than merely its magnitude (as done in the main text for simplicity). As described in the main text and above in the Methods section, the relative sign of J_x and B can be either positive or negative, reflecting whether the macroscopic spin is aligned or anti-aligned with respect to the applied magnetic field. For the case of this work, where caesium atoms are polarized in the $F = 4$ hyperfine manifold of the ground electronic state, positive $\mathrm{sgn}(J_x/B)$ corresponds

to a negative-mass oscillator (energy should be extracted to remove the ensemble from the fully polarized state), whereas negative $\mathrm{sgn}(J_x/B)$ corresponds to a positive-mass oscillator.

The presence of the static magnetic field adds the Hamiltonian term

$$\hat{H}_{\mathrm{S}} = \mu_{\mathrm{B}}g_F B\hat{J}_x \quad (21)$$

with μ_{B} being the Bohr magneton and $g_F = 1/4$ the Landé factor for the $F = 4$ manifold. In the language of spin oscillators, this Hamiltonian term affects the evolution of $\hat{X}_{\mathrm{S}}$ and $\hat{P}_{\mathrm{S}}$ in the following way:

$$\dot{\hat{X}}_{\mathrm{S}}|_B = \Omega_{\mathrm{S}}\hat{P}_{\mathrm{S}}; \quad \dot{\hat{P}}_{\mathrm{S}}|_B = -\Omega_{\mathrm{S}}\hat{X}_{\mathrm{S}} \quad (22)$$

where $\Omega_{\mathrm{S}} = -\mathrm{sgn}(J_x)\mu_{\mathrm{B}}g_F B$ so that $\Omega_{\mathrm{S}} > 0(<0)$ refers to the positive (negative) mass scenario.

A similar mapping can be performed with the Stokes components of light. For linearly polarized light in the x direction with Stokes component $S_x = \mathrm{sgn}(S_x)\Phi/2$, where Φ is the photon flux, the mapping can be written in the form:

$$\hat{X}_{\mathrm{L}} = \frac{\hat{S}_z}{\sqrt{|S_x|}}; \quad \hat{P}_{\mathrm{L}} = -\mathrm{sgn}(S_x)\frac{\hat{S}_y}{\sqrt{|S_x|}} \quad (23)$$

From equations (18), (20), (21), (23) and (27), we can write the Hamiltonian as:

$$\hat{H} = \sqrt{\Gamma_{\mathrm{S}}}\hat{X}_{\mathrm{S}}\hat{X}_{\mathrm{L}} + \Omega_{\mathrm{S}}(\hat{X}_{\mathrm{S}}^2 + \hat{P}_{\mathrm{S}}^2)/2 \quad (24)$$

The input–output relationships for the Stokes components

$$\hat{S}_{z,\mathrm{out}}(t) = \hat{S}_{z,\mathrm{in}}(t); \quad \hat{S}_{y,\mathrm{out}}(t) = \hat{S}_{y,\mathrm{in}}(t) + \alpha S_x\hat{J}_z(t) \quad (25)$$

are mapped into:

$$\hat{X}_{\mathrm{L,out}}(t) = \hat{X}_{\mathrm{L,in}}(t); \quad \hat{P}_{\mathrm{L,out}} = \hat{P}_{\mathrm{L,in}}(t) + \sqrt{\Gamma_{\mathrm{S}}}\hat{X}_{\mathrm{S}}(t) \quad (26)$$

where the readout rate Γ_{S} is:

$$\Gamma_{\mathrm{S}} = \frac{1}{2}\alpha^2\Phi|J_x| \quad (27)$$

The atomic spin dynamics, including the effects of its interaction with a Markovian reservoir, is

$$\frac{\mathrm{d}}{\mathrm{d}t}\hat{P}_{\mathrm{S}}(t) = -\Omega_{\mathrm{S}}\hat{X}_{\mathrm{S}}(t) - 2\gamma_{\mathrm{S}}\hat{P}_{\mathrm{S}}(t) + \sqrt{4\gamma_{\mathrm{S}}}\hat{F}_{\mathrm{S}}(t) + \sqrt{\Gamma_{\mathrm{S}}}\hat{X}_{\mathrm{L}}(t) \quad (28)$$

$$\frac{\mathrm{d}}{\mathrm{d}t}\hat{X}_{\mathrm{S}}(t) = \Omega_{\mathrm{S}}\hat{P}_{\mathrm{S}}(t) \quad (29)$$

with $\hat{F}_{\mathrm{S}}(t)$ being the random Langevin force acting on the spin; this force is the analogue of the thermal noise $\hat{f}$ that acts on the mechanical oscillator. Its correlation function is $\langle\hat{F}_{\mathrm{S}}(t)\hat{F}_{\mathrm{S}}(t')\rangle = \delta(t - t')(n_{\mathrm{S}} + 1/2)$, where a thermal spin occupancy $n_{\mathrm{S}} > 0$ reflects the excess noise induced by imperfect polarization of the ensemble. In the above analysis, the effect of tensor polarizability in the evolution of the light and spin state was neglected. For the detuning used in the experiment ($\Delta_{\mathrm{S}} \approx 3\,\mathrm{GHz}$) the effect of the tensor polarizability is estimated to be on the few per cent level[32].

In frequency space, the spin system is structurally identical to the one of the simple limit considered in equation (12) for the optomechanical system, that is, Fourier-transforming and solving equations (26), (28) and (29), one obtains the matrix relationship

$$\hat{\boldsymbol{X}}_{\mathrm{L,out}}^{\mathrm{S}}(\Omega) = \mathbb{S}(\Omega)\hat{\boldsymbol{X}}_{\mathrm{L,in}}(\Omega) + \sqrt{\Gamma_{\mathrm{S}}\gamma_{\mathrm{S}}}\chi_{\mathrm{S}}(\Omega)\hat{\boldsymbol{F}}_{\mathrm{S}}(\Omega)$$

where $\quad (30)$

$$\mathbb{S}(\Omega) = \begin{pmatrix} 1 & 0 \\ \Gamma_{\mathrm{S}}\chi_{\mathrm{S}}(\Omega) & 1 \end{pmatrix}$$

and the spin oscillator susceptibility is $\chi_{\mathrm{S}}(\Omega) = 2\Omega_{\mathrm{S}}/(\Omega_{\mathrm{S}}^2 - \Omega^2 - 2i\Omega\gamma_{\mathrm{S}})$. The spin thermal noise is represented by $\hat{\boldsymbol{F}}_{\mathrm{S}}(\Omega) = [0, \hat{F}_{\mathrm{S}}(\Omega)]^{\mathrm{T}}$. Here we adopt a phenomenological model for the susceptibility of the spin oscillator. A microscopic derivation along the lines of ref. 37 would result in a slightly different susceptibility with corrections to the present one scaling as Q_{S}^{-1} where $Q_{\mathrm{S}} \gg 1$ is the quality factor of the atomic oscillator.

Hybrid system. The two systems are connected such that $\hat{\boldsymbol{X}}_{\mathrm{L,in}}^{\mathrm{M}}(\Omega) = O_{\varphi}\hat{\boldsymbol{X}}_{\mathrm{L,out}}^{\mathrm{S}}(\Omega)$, as shown schematically in Extended Data Fig. 2. An optional phase shift φ

introduced deliberately in between the two systems is accounted for by the rotation matrix O_φ. Taking into account losses and further phase shifts as indicated in the figure, the compound transfer matrix for the hybrid optomechanical-spin system is:

$$\hat{\boldsymbol{X}}_{\mathrm{L,out}}(\Omega) = \underbrace{\sqrt{\eta_1\eta_2}\mathbb{M}(\Omega)O_\varphi\mathbb{S}(\Omega)\hat{\boldsymbol{X}}_{\mathrm{L,in}}(\Omega)}_{\text{vacuum noise of light transduced through S and M}} \tag{31}$$

$$+ \underbrace{\sqrt{\eta_1\eta_2}\mathbb{M}(\Omega)O_\varphi\sqrt{\Gamma_{\mathrm{S}}\gamma_{\mathrm{S}}}\chi_{\mathrm{S}}(\Omega)\hat{\boldsymbol{F}}_{\mathrm{S}}(\Omega)}_{\text{spin noise transduced through M}}$$

$$+ \underbrace{\sqrt{(1-\eta_1)\eta_2}\mathbb{M}(\Omega)\hat{\boldsymbol{V}}_{1,\mathrm{in}}(\Omega)}_{\text{vacuum noise of light from losses between S and M}}$$

$$+ \underbrace{\sqrt{\eta_2}\mathbb{V}(\Omega)\hat{\boldsymbol{V}}_{\mathrm{in}}(\Omega)}_{\text{vacuum noise of light from losses in optomechanical cavity}}$$

$$+ \underbrace{\sqrt{\eta_2}\mathbb{F}(\Omega)\hat{\boldsymbol{F}}(\Omega)}_{\text{thermal noise from M}}$$

$$+ \underbrace{\sqrt{1-\eta_2}\hat{\boldsymbol{V}}_{2,\mathrm{in}}(\Omega)}_{\text{vacuum noise from losses between M and detector}}$$

where η_1 and η_2 denote the transmission efficiencies from the spin system to the optomechanical cavity and from the optomechanical cavity to the detector, respectively. Vacuum noises incurred through these losses are described by $\hat{\boldsymbol{V}}_{1(2),\mathrm{in}}(\Omega)$.

Finally, the homodyne detection is performed in the frame of the classical field after the optomechanical system, where it has acquired a phase shift relative to the field before the optomechanical cavity. This phase is found as follows: the classical intracavity amplitude α is connected to the incoming amplitude α_{in} by

$$\alpha = \frac{\sqrt{2\kappa_1}}{\kappa - i\Delta}\alpha_{\mathrm{in}} = \frac{\alpha_{\mathrm{in}}}{\sqrt{\kappa^2+\Delta^2}}e^{i\phi}, \quad \phi = \arctan(\Delta/\kappa) \tag{32}$$

where $\kappa = \kappa_1 + \kappa_2$. The outgoing field is

$$\alpha_{\mathrm{out}} = -\alpha_{\mathrm{in}} + \sqrt{2\kappa_1}\alpha = \frac{\kappa_1 - \kappa_2 + i\Delta}{\kappa_1 + \kappa_2 - i\Delta}\alpha_{\mathrm{in}}$$

$$= \frac{[\kappa_1 - \kappa_2 + i\Delta][\kappa_1 + \kappa_2 + i\Delta]}{(\kappa_1 + \kappa_2)^2 + \Delta^2}\alpha_{\mathrm{in}} \propto e^{i(\psi+\phi)}\alpha_{\mathrm{in}}$$

where $\psi = \arctan(\Delta/(\kappa_1 - \kappa_2))$. Accordingly, the measured field quadrature $\hat{P}_{\mathrm{L,meas}}$ is determined by:

$$\begin{pmatrix} \hat{X}_{\mathrm{L,meas}} \\ \hat{P}_{\mathrm{L,meas}} \end{pmatrix} = O_{\psi+\phi}^{\mathrm{T}}\hat{\boldsymbol{X}}_{\mathrm{L,out}}(\Omega)$$

This relation is used to determine the measured noise spectral densities shown in the main text. For simplicity of notation, the measured quadrature $\hat{P}_{\mathrm{L,meas}}$ is referred to as $\hat{P}_{\mathrm{L,out}}$ in the main text and other parts of the Methods.

We will now use the transfer matrix of the hybrid system to analyse the QBA contribution to the optical output field (equation (31), first line). For the case when the optomechanical damping dominates the membrane response, $\gamma_{\mathrm{M}} \gg \gamma_{\mathrm{M0}}$, and in the sideband unresolved limit, $\Omega_{\mathrm{M}} \ll \kappa$, we can apply the approximate optomechanical scattering matrix, equation (17), to find (ignoring optical losses $\eta_1 = 0 = \eta_2$, setting $\kappa_2 = 0$ and $\varphi = 0$ for simplicity)

$$\hat{P}_{\mathrm{L,meas}} = [\Gamma_{\mathrm{M}}L_0^2\chi_{\mathrm{M}}(\Omega) + \Gamma_{\mathrm{S}}\chi_{\mathrm{S}}(\Omega)\{1 + i\Gamma_{\mathrm{M}}\chi_{\mathrm{M}}(\Omega)L_0\delta L\}]\hat{X}_{\mathrm{L,in}} \tag{33}$$

where L_0 is the empty cavity Lorentzian response and δL is the difference in cavity response at frequencies $\pm\Omega \ll \kappa$. Only with $\delta L = 0$ (LO$_2$ tuned to cavity resonance) do the spin QBA and the mechanical QBA add/subtract in $\hat{P}_{\mathrm{L,meas}}$. From equations (3), (7) and (9), one finds that $L_0\delta L = (\gamma_{\mathrm{M}} - \gamma_{\mathrm{M0}})/\Gamma_{\mathrm{M}}$, that is the distortion of the QBA due to $\delta L \neq 0$ has the same origin as the optomechanical broadening. In the relevant case of strong optomechanical cooling $\gamma_{\mathrm{M}} \gg \gamma_{\mathrm{M0}}$, there is no back-action cancellation at the exact joint resonance frequency since $i\chi_{\mathrm{M}}(\Omega = \Omega_{\mathrm{M}})\gamma_{\mathrm{M}} = -1$.

In this regime the QBA power spectrum of the hybrid system $S_{P_{\mathrm{L,meas}}}$ corresponding to equation (33) becomes

$$S_{P_{\mathrm{L,meas}}} = \frac{(\Gamma_{\mathrm{M}}L_0^2\delta_{\mathrm{S}} + \Gamma_{\mathrm{S}}\delta_{\mathrm{M}})^2 + \Gamma_{\mathrm{M}}^2L_0^4\gamma_{\mathrm{S}}^2}{(\delta_{\mathrm{M}}^2 + \gamma_{\mathrm{M}}^2)(\delta_{\mathrm{S}}^2 + \gamma_{\mathrm{S}}^2)}S_{X_{\mathrm{L,in}}} \tag{34}$$

with $\delta_{\mathrm{M,S}} = \Omega - \Omega_{\mathrm{M,S}}$ and $S_{X_{\mathrm{L,in}}}$ being the power spectral density of the input light amplitude fluctuations. For matched responses $\Gamma_{\mathrm{S}} = \Gamma_{\mathrm{M}}L_0^2$, $\Omega_{\mathrm{M}} = \Omega_{\mathrm{S}}$, $\gamma_{\mathrm{M}} = \gamma_{\mathrm{S}}$, the ratio of the hybrid QBA spectrum to the QBA spectrum of the mechanics becomes $\gamma_{\mathrm{M}}^2/((\Omega - \Omega_{\mathrm{M}})^2 + \gamma_{\mathrm{M}}^2)$, thus QBA evasion is indeed expected everywhere, except for $\Omega = \Omega_{\mathrm{M}}$, as indeed observed in Fig. 2 and described in the main text. The minimal variance of the hybrid QBA is 1/2 of the QBA of the mechanical oscillator alone.

Calibration of QBA for the spin system. To characterize the quantum cooperativity, $C_{\mathrm{q}}^{\mathrm{S}}$, and the readout rate, Γ_{S}, one can use the fact that a single light quadrature is coupled to the oscillator: by suitable modulation of $\hat{X}_{\mathrm{L,in}}$, one can boost the contribution of the measurement-induced back-action.

As thoroughly discussed in the previous sections and summarized by equation (30), the input–output relations for the continuous readout of a harmonic oscillator are

$$\begin{pmatrix} \hat{X}_{\mathrm{L,out}} \\ \hat{P}_{\mathrm{L,out}} \end{pmatrix} = \begin{pmatrix} \hat{X}_{\mathrm{L,in}} \\ \hat{P}_{\mathrm{L,in}} \end{pmatrix} + \Gamma v_1^{\mathrm{T}}Lv_2\begin{pmatrix} 0 & 0 \\ 1 & 0 \end{pmatrix}\begin{pmatrix} \hat{X}_{\mathrm{L,in}} \\ \hat{P}_{\mathrm{L,in}} \end{pmatrix} + \sqrt{\Gamma\gamma}v_1^{\mathrm{T}}L\hat{F}_{\mathrm{Th}}\begin{pmatrix} 0 \\ 1 \end{pmatrix} \tag{35}$$

in which Γ is the readout rate, γ the decay rate and:

$$L = (i\omega\mathbb{1} - M)^{-1}$$
$$M = \begin{pmatrix} 0 & \omega_0 \\ -\omega_0 & -\gamma \end{pmatrix}$$
$$v_1 = \begin{pmatrix} 1 \\ 0 \end{pmatrix} \quad v_2 = \begin{pmatrix} 0 \\ 1 \end{pmatrix}$$

In a more straightforward language, equation (35) becomes

$$\begin{pmatrix} \hat{X}_{\mathrm{L,out}} \\ \hat{P}_{\mathrm{L,out}} \end{pmatrix} = \begin{pmatrix} \hat{X}_{\mathrm{L,in}} \\ \hat{P}_{\mathrm{L,in}} \end{pmatrix} + R_{\mathrm{BA}}\begin{pmatrix} 0 & 0 \\ 1 & 0 \end{pmatrix}\begin{pmatrix} \hat{X}_{\mathrm{L,in}} \\ \hat{P}_{\mathrm{L,in}} \end{pmatrix} + R_{\mathrm{Th}}\begin{pmatrix} 0 \\ 1 \end{pmatrix} \tag{36}$$

with R_{BA} and R_{Th} being the response functions of the oscillator to the back-action and thermal forces.

The effect of losses is also important, as there is an admixture of uncorrelated vacuum, indicated by the subscript v, with the signal of interest, therefore:

$$\begin{pmatrix} \hat{X}_{\mathrm{L,out}} \\ \hat{P}_{\mathrm{L,out}} \end{pmatrix} \rightarrow \sqrt{\eta}\begin{pmatrix} \hat{X}_{\mathrm{L,out}} \\ \hat{P}_{\mathrm{L,out}} \end{pmatrix} + \sqrt{1-\eta}\begin{pmatrix} \hat{X}_{\mathrm{L,v}} \\ \hat{X}_{\mathrm{L,v}} \end{pmatrix} \tag{37}$$

The PSD for both light quadratures are calculated from the absolute square of equation (36):

$$S_{XX} = \eta\langle\hat{X}_{\mathrm{L,in}}\hat{X}_{\mathrm{L,in}}^\dagger\rangle + (1-\eta)\langle\hat{X}_{\mathrm{L,v}}\hat{X}_{\mathrm{L,in}}^\dagger\rangle$$
$$S_{PP} = \eta[\langle\hat{P}_{\mathrm{L,in}}\hat{P}_{\mathrm{L,in}}^\dagger\rangle + R_{\mathrm{BA}}^2\langle\hat{X}_{\mathrm{L,in}}\hat{X}_{\mathrm{L,in}}^\dagger\rangle + R_{\mathrm{Th}}^2] + (1-\eta)\langle\hat{P}_{\mathrm{L,v}}\hat{P}_{\mathrm{L,v}}^\dagger\rangle \tag{38}$$

Therefore, it is explicit that to boost the back-action component of the oscillator readout in comparison to the other noise contributions, one should modulate the in-phase quadrature of light, $\hat{X}_{\mathrm{L}}$. Doing so, the input spectral densities are

$$\langle\hat{X}_{\mathrm{L,in}}\hat{X}_{\mathrm{L,in}}^\dagger\rangle \rightarrow (n_{\mathrm{WN}}+1)\langle\hat{X}_{\mathrm{L,in}}\hat{X}_{\mathrm{L,in}}^\dagger\rangle \text{ and } \langle\hat{X}_{\mathrm{L},i}(\omega)\hat{X}_{\mathrm{L},j}^\dagger(-\omega')\rangle = \delta(\omega-\omega')\delta_{ij},$$

in which i,j represent the different sources of fluctuations. Therefore, the input–output relations from equation (38) are:

$$S_{XX} = \eta n_{\mathrm{WN}} + 1$$
$$S_{PP} = \eta[R_{\mathrm{BA}}^2(n_{\mathrm{WN}}+1) + R_{\mathrm{Th}}^2] + 1 \tag{39}$$

Experimentally, to be able to calculate the back-action to thermal noise ratio, one needs to measure (i) the response of the system to SN drive and (ii) the response of the system with some known modulation n_{WN}, for a given probe power. Calibrating the curves in SN units, the measured spectral on-resonance heights after the subtraction of the WN contribution, defined here as A and B, are

$$S_{PP}^{\mathrm{WN}} - 1 = B = \eta[R_{\mathrm{BA}}^2(n_{\mathrm{WN}}+1) + R_{\mathrm{Th}}^2]$$
$$S_{PP}^{\mathrm{SN}} - 1 = A = \eta[R_{\mathrm{BA}}^2 + R_{\mathrm{Th}}^2]$$

therefore, the desired ratio is:

$$\frac{R_{\text{BA}}^2}{R_{\text{Th}}^2} = \frac{B - A}{(n_{\text{WN}} + 1)A - B} \tag{40}$$

This technique was used to calibrate C_{q}^{S}, the quantum cooperativity of the spin oscillator. For this measurement, $\eta = 0.7$ is the detection efficiency, S_{PP}^{WN} is the spectral density of added WN in units of vacuum noise, and S_{QBA} and S_{Th} are the back-action and thermal spectral densities, respectively. The measurements of the phase noise presented in Fig. 2c and of S_{PP}^{WN} are performed with polarization interferometry using LO_1 calibrated to the SN of LO_1. From the phase noise S_{PP}^{SN} and S_{PP}^{WN} measured for $n_{\text{WN}} = 0$ (vacuum input) and $S_{\text{WN}} = 1.2$, respectively (Fig. 2c), we find $S_{\text{QBA}} = (S_{PP}^{\text{WN}} - S_{PP}^{\text{SN}})/(1.2 \times \eta_A)$ and $C_{\text{q}}^{\text{S}} = (S_{PP}^{\text{WN}} - S_{PP}^{\text{SN}})/(2.2 \times S_{PP}^{\text{WN}} - S_{PP}^{\text{SN}})$ $= 1.10 \pm 0.15$.

Data availability. Source Data for Figs 2–4 are available in the online version of the paper. Other data for this study are available from the corresponding author upon request.

30. Corsini, E. P., Karaulanov, T., Balabas, M. & Budker, D. Hyperfine frequency shift and Zeeman relaxation in alkali-metal-vapor cells with antirelaxation alkene coating. *Phys. Rev. A* **87,** 022901 (2013).
31. Borregaard, J. *et al.* Scalable photonic network architecture based on motional averaging in room temperature gas. *Nat. Commun.* **7,** 11356 (2016).
32. Jensen, K. *Quantum Information, Entanglement and Magnetometry with Macroscopic Samples and Non-classical Light.* PhD dissertation, Univ. Copenhagen (2011).
33. Holstein, T. & Primakoff, H. Field dependence of the intrinsic domain magnetization of a ferromagnet. *Phys. Rev.* **58,** 1098–1113 (1940).
34. Jayich, A. M. *et al.* Dispersive optomechanics: a membrane inside a cavity. *New J. Phys.* **10,** 095008 (2008).
35. Wilson, D. J., Regal, C. A., Papp, S. B. & Kimble, H. J. Cavity optomechanics with stoichiometric SiN films. *Phys. Rev. Lett.* **103,** 207204 (2009).
36. Marquardt, F., Chen, J. P., Clerk, A. A. & Girvin, S. M. Quantum theory of cavity-assisted sideband cooling of mechanical motion. *Phys. Rev. Lett.* **99,** 093902 (2007).
37. Vasilyev, D. V., Hammerer, K., Korolev, N. & Sørensen, A. S. Quantum noise for Faraday light matter interfaces. *J. Phys. At. Mol. Opt. Phys.* **45,** 124007 (2012).
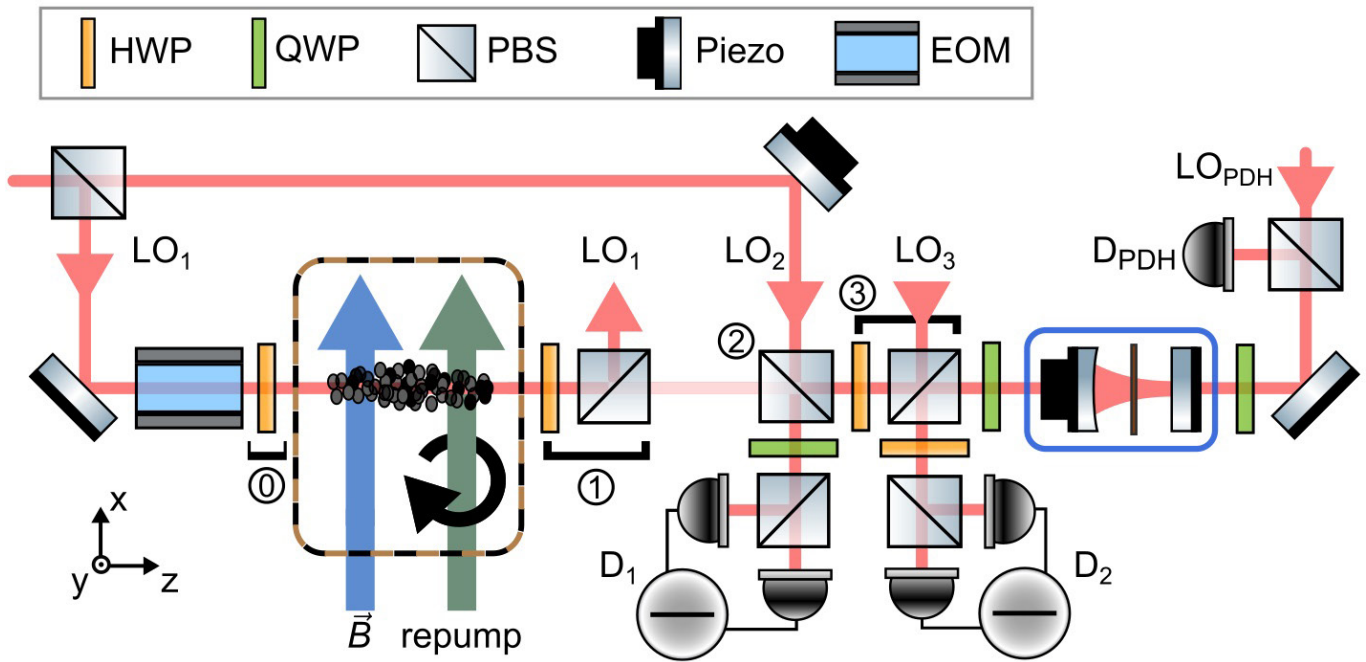
Extended Data Figure 1 | Detailed schematic of the experimental set-up. The atomic spin system is pictured in the black–orange dashed box (left), along with its *B* field and optical pumping (blue and olive arrows; bottom); the optomechanical membrane-in-the-middle set-up is in the blue box (right). Circled numerals indicate sections with specific functions. The hybrid system is probed via a travelling optical mode (pink lines and arrows). The atomic system, driven by local oscillator 1 (LO_1) with linear polarization angle set by section (0), has its output polarization filtered in section (1) and is recombined with the correct phase with LO_2 in section (2), set electronically via suitable detection in D_1; the apparatus in section (3) ensures that both local oscillator and the filtered atomic response have the same polarization. The optomechanical system is probed by LO_2 in reflection and phase-sensitive detection is done via homodyning with LO_3 in D_2. Probing the remaining cavity port in reflection with LO_{PDH}, the optomechanical system is frequency stabilized using the Pound–Drever–Hall (PDH) technique on the signal of detector D_{PDH}. HWP, half-wave plate; QWP, quarter-wave plate; PBS, polarizing beamsplitter; EOM, electro-optic modulator. See Methods for details.
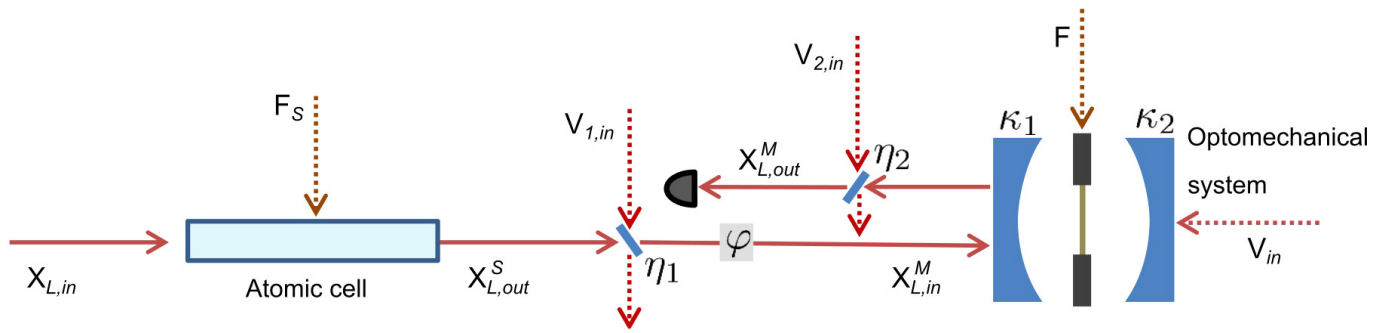
Extended Data Figure 2 | Theoretical schematic of the set-up. The atomic spin (in the spin cell, blue box at left) is driven by light noise $X_{L,in}$ and spin noise F_S. Output light of the spin system $X^S_{L,out}$ is channelled to the optomechanical system. En route, it experiences losses characterized by a transmissivity η_1 associated with additional light noise $V_{1,in}$ and a phase rotation by an angle φ, resulting in a driving field $X^M_{L,in}$ of the optomechanical system. The optomechanical cavity (shown blue at right) is two-sided, with decay rates κ_1 and κ_2. The optomechanical system is driven in addition by light noise V_{in} and a thermal force F. The output field of the optomechanical system experiences further losses, with transmissivity η_2 associated with additional light noise $V_{2,in}$. All unwanted additional noise sources are indicated with dashed lines.

Extended Data Table 1 | Summary of notation and experimental parameters

Parameter	Symbol	Value (Fig. 2&3, Fig. 4)
Atomic spin oscillator		
Intrinsic decoherence rate	γ_{S0}	$2\pi \times 500$ Hz
Total decoherence rate	γ_S	$2\pi \times (2.6, 2.3)$ kHz
LO_1 driving power		$(1.7, 1.5)$ mW
Readout rate	Γ_S	$2\pi \times (70, 60)$ kHz
Detuning from the D_2 $F = 4 \rightarrow F' = 5$ transition	Δ_S	3 GHz
Quantum cooperativity	C_q^S	1.10 ± 0.15
Spin Polarization		60%
Microcell optical losses	$\eta_{microcell}$	13%
Microcell temperature		65°C
Mechanical oscillator		
Effective mass	m_{eff}	14 ng
Zero point fluctuations	x_{zpf}	1 fm
Intrinsic mechanical frequency	Ω_{M0}	$2\pi \times 1.28$ MHz
Intrinsic damping rate	γ_{M0}	$2\pi \times 50$ mHz
Optical damping rate	$\gamma_{M,opt}$	$2\pi \times (2.8, 2.7)$ kHz
Optical mechanical frequency shift		$2\pi \times (-12, -11)$ kHz
Cavity detuning	Δ	$2\pi \times -4.7$ MHz
Total cavity half linewidth	κ	$2\pi \times (8.7, 7.7)$ MHz
LO2 drive power		$(54, 38)$ µW
Intracavity photons	N	$(5.8, 4.4) \times 10^6$
Single photon coupling rate	g_0	$2\pi \times 210$ Hz
Thermal bath temperature	T_{bath}	7 K
Bath occupancy	n_{bath}	114×10^3
Mean thermal occupancy	$\bar{n}_M^{th}$	2.1
Quantum cooperativity	C_q^M	$(2.6, 2.2)$
Hybrid & detection		
Quantum efficiency between systems	η_1	61%
Detection efficiency (amplitude quadrature)	η_2	72%, 75%
Detection efficiency (phase quadrature)	η_2	64%, 67%
Homodyning visibility		89%
Cavity mode-matching	η_{mm}	89%

Values in the rightmost column are for data shown in Figs 2–4.